

Solid-State ^{127}I NMR and GIPAW DFT Study of Metal Iodides and Their Hydrates: Structure, Symmetry, and Higher-Order Quadrupole-Induced Effects

Cory M. Widdifield and David L. Bryce*

Department of Chemistry and Centre for Catalysis Research and Innovation, University of Ottawa, 10 Marie Curie Pvt., Ottawa, Ontario, Canada

Received: August 30, 2010

Central-transition ^{127}I solid-state nuclear magnetic resonance (SSNMR) spectra are presented for several anhydrous group 2 metal iodides (MgI_2 , CaI_2 , SrI_2 , and BaI_2), hydrates ($\text{BaI}_2 \cdot 2\text{H}_2\text{O}$ and $\text{SrI}_2 \cdot 6\text{H}_2\text{O}$), and CdI_2 (4H polytype). Variable offset cumulative spectrum data acquisition coupled with echo pulse sequences and an ‘ultrahigh’ applied field of 21.1 T were usually suitable to acquire high-quality spectra. Spectral analysis revealed iodine-127 nuclear quadrupole coupling constants ($C_Q(^{127}\text{I})$) ranging in magnitude from 43.5 (CaI_2) to 214 MHz (one site in SrI_2). For very large C_Q , analytical second-order perturbation theory could not be used to reliably extract chemical shifts and a treatment which includes quadrupolar effects exactly was required (Bain, A. D. *Mol. Phys.* **2003**, *101*, 3163). Differences between second-order and exact modeling allowed us to observe ‘higher-order’ quadrupole-induced effects for the first time. This finding will have implications for the interpretation of SSNMR spectra of quadrupolar nuclei with large quadrupole moments. In favorable situations (i.e., $C_Q(^{127}\text{I}) < 120$ MHz), measurements were also performed at 11.75 T which when combined with the 21.1 T data allowed us to measure iodine chemical shift (CS) tensor spans in the range from 60 ($\text{BaI}_2 \cdot 2\text{H}_2\text{O}$) to 300 ppm (one site in BaI_2). These measurements represent the first complete characterizations (i.e., electric field gradient and CS tensors as well as their relative orientation) of noncubic iodide sites using ^{127}I SSNMR. In select cases, the SSNMR data are supported with ^{127}I NQR measurements. We also summarize a variety of trends in the halogen SSNMR parameters for group 2 metal halides. Gauge-including projector-augmented wave DFT computations are employed to complement the experimental observations, to predict potential structures for the two hydrates, and to highlight the sensitivity of $C_Q(^{127}\text{I})$ to minute structural changes, which has potential applications in NMR crystallography.

Introduction

Iodine, found naturally in seawater, minerals, kelp, and the brines associated with oil and gas wells, finds use in a number of industrial and consumer products (e.g., food stabilizers, animal feed supplements, disinfectants, inks, dyes, and pharmaceuticals).¹ Likewise, numerous important chemical compounds contain the iodide anion (I^-). For example, NaI promotes amine carbonylation reactions,² bis(trimethylammonium) alkane diiodides can resolve mixtures of key intermediates which are used in the synthesis of fluorochemicals and fluoropolymers,³ and SmI_2 has recently been touted as “one of the premier single-electron reducing agents in synthetic chemistry”.⁴ In addition, there are several important hypervalent I(III) - and I(V) -containing reagents: *o*-iodoxybenzoic acid is used in the synthesis of α -aminoaldehydes and carbon–heteroatom oxidations,⁵ and the ‘Togni reagent’ is used in the electrophilic addition of CF_3 moieties to carbon- and sulfur-centered nucleophiles.⁶

While many chemical properties of the halogens are similar, their nuclear properties differ significantly; hence, development of their corresponding solid-state nuclear magnetic resonance (SSNMR) methods is rather distinct. Fluorine-19 SSNMR spectroscopy is a highly developed characterization tool with well-established applications.^{7–9} While the SSNMR spectroscopy of the remaining halogens is substantially less developed

relative to ^{19}F , several recent applications of $^{35/37}\text{Cl}$ and $^{79/81}\text{Br}$ SSNMR spectroscopy toward the study of chlorine- and bromine-containing systems have been published. Since 2006, $^{35/37}\text{Cl}$ SSNMR experiments have been used to study a variety of systems, including (i) group 4 organometallic^{10,11} and group 13 inorganic materials,¹² (ii) antiferromagnetic materials,^{13–16} (iii) superconductors,¹⁷ (iv) amino acid hydrochlorides,^{18,19} and (v) ionic liquids.^{20,21} The utility of $^{35/37}\text{Cl}$ SSNMR experiments at detecting the presence of (i) hydration states in group 2 metal chlorides²² and (ii) polymorphs^{23,24} has also been demonstrated. During the same period, $^{79/81}\text{Br}$ SSNMR spectroscopy has been used to study *n*-alkyltrimethylammonium bromides,²⁵ group 2 metal bromides,²⁶ and ionic liquids.²¹ Bromine SSNMR experiments also provided key data that were used to propose a modified MgBr_2 crystal structure.²⁷ Unlike $^{35/37}\text{Cl}$ and $^{79/81}\text{Br}$, development of ^{127}I SSNMR has nearly reached a standstill. Other than a study on the dynamical structure of $\gamma\text{-Ag}_x\text{Cu}_{1-x}\text{I}^{28}$ and brief mentions within reports on ionic liquids²¹ and pulse sequence advances,²⁹ there have been no applications of ^{127}I SSNMR since 2001.³⁰ As no substantial ^{127}I SSNMR account has been published in nearly a decade, a systematic ^{127}I SSNMR study employing modern techniques and apparatus does not exist. In fact, aside from the trivial cases involving cubic environments, no iodide site has ever been fully characterized (i.e., quantification of both the chemical shift and electric field gradient (EFG) tensors) using ^{127}I SSNMR.

The ^{127}I nucleus is 100% naturally abundant, possesses a magnetogyric ratio (γ) slightly less than that of ^{13}C , and is

* To whom correspondence should be addressed. Phone: +1 613 562 5800 ext. 2018. Fax: +1 613 562 5170. E-mail: dbryce@uottawa.ca.

quadrupolar (i.e., $I > 1/2$; $I(^{127}\text{I}) = 5/2$). The primary experimental challenge associated with using the ^{127}I nucleus as a SSNMR probe is its moderately large nuclear electric quadrupole moment ($Q(^{127}\text{I}) = -6.96 \times 10^{-29} \text{ m}^2$).³¹ Any nucleus possessing a nonzero Q has the potential to be used as a probe of the local EFG, but the coupling between the Q and the EFG at the nucleus, referred to as the quadrupolar interaction (QI), broadens the SSNMR signal in powdered samples.³² In cases where the QI is moderately small, this broadening provides significant information regarding the local electronic structure in molecules and crystalline materials.³³ For cases where the QI is large, the broadening may be such that the SSNMR signal is undetectable. Of the naturally occurring isotopes where $Z < 61$, only the $^{113/115}\text{In}$ nuclides possess Q values larger than ^{127}I ; hence, the acquisition of high-quality ^{127}I SSNMR spectra is a challenge. As second-order quadrupolar line shape broadening scales inversely with applied magnetic field (B_0), a potential remedy is to conduct the SSNMR experiments within an ‘ultrahigh’ B_0 (i.e., $> 18.8 \text{ T}$).

We present here a ^{127}I SSNMR study of a variety of MI_2 and MI_2 hydrates and highlight the information that can be gained by conducting ^{127}I SSNMR experiments in both standard and ultrahigh fields. Unlike ^{127}I nuclear quadrupole resonance (NQR) experiments, isotropic chemical shifts (δ_{iso}) and chemical shift anisotropy (CSA) are potential observables in ^{127}I SSNMR spectra; hence, the SSNMR spectra are possibly richer in information. Using exact theory,³⁴ modeling of SSNMR signals where the high-field approximation (commonly made when fitting SSNMR line shapes of quadrupolar nuclei) is not clearly valid is performed for the first time on powdered samples. In this regime, we observe ‘higher-order’ quadrupole-induced effects (QIE) on the SSNMR line shapes and support our SSNMR observations with ^{127}I NQR measurements. This finding will likely have consequences for the future interpretation of SSNMR spectra of large- Q nuclei (e.g., $^{47/49}\text{Ti}$, ^{59}Co , $^{79/81}\text{Br}$, $^{113/115}\text{In}$, ^{209}Bi , etc.) in low-symmetry environments. We also discuss the ability of ^{127}I SSNMR experiments to probe hydration states in group 2 metal iodide hydrates and comment upon several halogen SSNMR parameter trends across the group 2 metal halides and group 2 metal halide hydrates. Experimental observations are complemented with gauge-including projector-augmented wave (GIPAW) density functional theory (DFT) calculations, and we comment upon the ability of these computations to reproduce the observed NMR parameter values.

Experimental Section

1. Sample Preparation. MgI_2 (99.998%), CaI_2 (99.95%), SrI_2 ($\geq 99.99\%$), BaI_2 (99.995%), CdI_2 (99.999%), $\text{SrI}_2 \cdot 6\text{H}_2\text{O}$ ($\geq 99.99\%$), and $\text{BaI}_2 \cdot 2\text{H}_2\text{O}$ (98%) were purchased from Sigma-Aldrich. All anhydrous compounds were received as beads, except SrI_2 , which was a powder. All hydrates were received as powders. Sample purity was confirmed for each compound by the manufacturer (see the Supporting Information). As all compounds are hygroscopic and light sensitive, they were stored and prepared for use in minimal light conditions under either dry N_2 or Ar, except CdI_2 , which was stored in a dry, dark cabinet. $\text{BaI}_2 \cdot 2\text{H}_2\text{O}$ was found to be air stable for an extended period under low-humidity conditions. Prior to ^{127}I SSNMR/NQR experiments, samples were powdered and tightly packed into 3.2, 4, or 7 mm o.d. Bruker magic angle spinning (MAS) ZrO_2 rotors.

2. Solid-State ^{127}I NMR. Data were primarily acquired at the National Ultrahigh-field NMR Facility for Solids in Ottawa using a standard bore (54 mm) Bruker AVANCE II spectrometer

operating at $B_0 = 21.1 \text{ T}$ ($\nu_0(^1\text{H}) \approx 900.08 \text{ MHz}$). Additional ^{127}I SSNMR data were acquired at the University of Ottawa using a wide bore (89 mm) Bruker AVANCE spectrometer operating at $B_0 = 11.75 \text{ T}$ ($\nu_0(^1\text{H}) \approx 500.13 \text{ MHz}$). At 21.1 T, experiments used 3.2 or 4 mm Bruker HX MAS probes ($\nu_0(^{127}\text{I}) \approx 180.08 \text{ MHz}$), while at 11.75 T, experiments used a 4 mm Bruker HXY MAS probe ($\nu_0(^{127}\text{I}) \approx 100.06 \text{ MHz}$). All spectra were referenced to 0.1 mol/dm³ KI in D_2O at 0 ppm³⁵ using NaI or KI as secondary standards ($\delta_{\text{iso}}(\text{NaI(s)}) = 226.71 \text{ ppm}$, $\delta_{\text{iso}}(\text{KI(s)}) = 192.62 \text{ ppm}$).³⁶ Iodine $\pi/2$ pulse widths were established using the ^{127}I SSNMR signals of powdered KI or NaI under 10 kHz MAS. NaI and KI are cubic salts; hence, the central transition (CT) selective (i.e., ‘solid $\pi/2$ ’) pulse widths used for all samples under study were scaled by $1/(I + 1/2) = 1/3$, relative to the $\pi/2$ pulse width determined using the cubic salts.

Iodine-127 SSNMR signals were primarily acquired using either Solomon echo (i.e., $\pi/2 - \tau_1 - \pi/2 - \tau_2 - \text{acq}$)^{37–39} or Hahn echo (i.e., $\pi/2 - \tau_1 - \pi - \tau_2 - \text{acq}$)⁴⁰ pulse sequences. Typical parameters were as follows: $\pi/2 = 1.0 \mu\text{s}$ ($\pi = 2.0 \mu\text{s}$); spectral window = 2 MHz; $\tau_1 = 18.6\text{--}30 \mu\text{s}$; $\tau_2 = 4.3\text{--}20 \mu\text{s}$; and 512 or 1024 complex time-domain data points were collected. Wide band uniform-rate smooth truncation (WURST) echo experiments⁴¹ on SrI_2 used a 1 MHz sweep bandwidth via a $50 \mu\text{s}$ WURST pulse shape.^{42,43} For all experiments, 4000–18 800 transients were acquired with a pulse delay of typically 0.25 s. For $\text{BaI}_2 \cdot 2\text{H}_2\text{O}$, continuous wave ^1H decoupling was tested ($\nu_1(^1\text{H}) \approx 85 \text{ kHz}$). Due to the line width associated with the ^{127}I SSNMR signal for $\text{SrI}_2 \cdot 6\text{H}_2\text{O}$ at 21.1 T (i.e., $\Delta\nu > 3 \text{ MHz}$), ^1H decoupling was not required. For full experimental details, see the Supporting Information, Table S1.

Variable offset cumulative spectrum (VOCS) data acquisition methods^{44–46} were usually required to acquire the ^{127}I SSNMR signals. Offsets were 200–300 and 848 kHz for Solomon/Hahn echo and WURST echo experiments, respectively. Each processed component spectrum (‘subspectrum’) was combined in the frequency domain by coaddition to produce the total spectrum.

3. Solid-State ^{127}I NQR. Experiments used either a 4 mm Bruker HXY MAS probe or a 7 mm Bruker HX static probe and were performed to confirm the measured ^{127}I EFG parameters for selected compounds. Spectra were acquired using the Hahn echo pulse sequence. Short ($< 2 \mu\text{s}$), high-power pulses were used as the transmitter frequency was varied until the resonances were found. Typical offsets while searching for the NQR signals were 200 kHz. For further details, see the Supporting Information, Table S1.

4. NMR/NQR Line Shape Fitting and Parameter Determination. The SSNMR spectra were typically modeled using analytical simulation software (WSolids1)⁴⁷ and include contributions from the QI to second-order and CSA under the high-field approximation. Other contributions (i.e., J , dipole–dipole, etc.) are insignificant. In cases where the high-field approximation was not obviously valid (vide infra), line shape analysis was performed using a simulation program that incorporates QI effects exactly.³⁴ The observed ^{127}I SSNMR signals primarily correspond to the CT ($m_I = +1/2 \leftrightarrow -1/2$), but effects due to the satellite transitions (ST; $m_I = \pm 3/2 \leftrightarrow \pm 1/2$ and $\pm 5/2 \leftrightarrow \pm 3/2$, $\Delta m_I = \pm 1$) were included in all simulations. As the ST are generally time consuming to measure experimentally, they were collected only for CaI_2 .

The EFG is described using a traceless, symmetric second-rank tensor (\vec{V}). In its own principal axis system (PAS), \vec{V} may be represented using a diagonal 3×3 Cartesian matrix. The

TABLE 1: Experimental ^{127}I EFG and Chemical Shift Tensor Parameters: Anhydrous Metal Iodides^a

compound	site label	$ C_Q(^{127}\text{I}) /\text{MHz}$	η_Q	$\delta_{\text{iso}}/\text{ppm}$	Ω/ppm	κ	α/deg	β/deg	γ/deg	notes
MgI_2	—	79.8(0.5)	0.02(0.02)	920(50)	120(80)	-1^c	90^d	90(20)	0^d	—
CaI_2	—	43.5(0.3)	0.02(0.02)	755(10)	<50	—	—	—	—	—
SrI_2	I(1)	105.2(0.7)	0.467(0.012)	880(70)	—	—	—	—	—	—
	I(2)	214.0(0.1) ^e	0.316(0.002) ^e	720(150) ^f	—	—	—	—	—	NQR: $\nu_1 = 35.415(0.015)$; $\nu_2 = 62.980(0.015)^g$
BaI_2	I(1)	96.2(0.8)	0.175(0.015)	650(70) ^f	300(100)	< -0.5	0^d	45(20)	180 ^d	—
	I(2)	120.9(0.2) ^e	0.015(0.015) ^e	1000(80) ^f	—	—	—	—	—	NQR: $\nu_1 = 18.13(0.02)$; $\nu_2 = 36.26(0.02)$
CdI_2 (4H)	—	95.7(1.0)	0^c	1450(100)	—	—	—	—	—	one-site model
CdI_2 (4H)	I(1)	95.7(1.0)	0^c	1450(100)	—	—	—	—	—	two-site model
	I(2)	97.5(1.0)	0^c	1420(100)	—	—	—	—	—	

^a Error bounds are in parentheses. Parameter definitions are in the main text. ^b While C_Q may take any real value, $|C_Q|$ is measured using these SSNMR experiments. ^c Assumed, based upon the crystallographic site symmetry. ^d Simulated SSNMR line shape is insensitive to parameter variation. The assigned value is based on computational results. ^e Established with the aid of ^{127}I NQR experiments. ^f Established with the aid of exact simulation software. ^g All ^{127}I NQR frequencies are in MHz.

diagonal elements (V_{ii}) are known as the principal components and are defined such that $|V_{11}| \leq |V_{22}| \leq |V_{33}|$. The nuclear quadrupole coupling constant (C_Q) and asymmetry parameter (η_Q) are related to the principal components: $C_Q = eQV_{33}/h$; $\eta_Q = (V_{11} - V_{22})/V_{33}$, where C_Q is in frequency units and η_Q is unitless, ranging between 0 and 1.

Magnetic shielding may be adequately described^{48–50} using a symmetric second-rank tensor ($\tilde{\sigma}$), with a trace equal to the isotropic magnetic shielding (σ_{iso}). In its own PAS, $\tilde{\sigma}$ is specified using three principal components (σ_{ii}), defined such that $\sigma_{11} \leq \sigma_{22} \leq \sigma_{33}$. The $\tilde{\sigma}$ may be described by the following parameters (Maryland convention): $\sigma_{\text{iso}} = (\sigma_{11} + \sigma_{22} + \sigma_{33})/3$; $\Omega \equiv \sigma_{33} - \sigma_{11}$ (span); $\kappa \equiv 3(\sigma_{33} - \sigma_{22})/\Omega$ (skew), where σ_{iso} is in ppm, Ω is a positive value in ppm, and κ is unitless, ranging from -1 to $+1$.^{51,52} The $\tilde{\sigma}$ in solids cannot generally be measured experimentally; rather, the chemical shift tensor ($\tilde{\delta}$) is measured. All $\tilde{\sigma}$ elements (σ_{ij}) may be related to $\tilde{\delta}$ elements (δ_{ij}), as $\delta_{ij} = (\sigma_{\text{ref,iso}} - \sigma_{ij})/(1 - \sigma_{\text{ref,iso}})$, where $\sigma_{\text{ref,iso}}$ is the isotropic shielding value of the reference. In the $\tilde{\delta}$ PAS, $\delta_{11} \geq \delta_{22} \geq \delta_{33}$; $\delta_{\text{iso}} = (\delta_{11} + \delta_{22} + \delta_{33})/3$; $\Omega = (\delta_{11} - \delta_{33})(1 - \sigma_{\text{ref,iso}}) \approx (\delta_{11} - \delta_{33})$; $\kappa \equiv 3(\delta_{22} - \delta_{\text{iso}})/(\delta_{11} - \delta_{33}) \approx 3(\delta_{22} - \delta_{\text{iso}})/\Omega$.⁵³

When both QI and CSA effects are observed, it may be possible to determine the relative orientation of the \tilde{V} and $\tilde{\sigma}$ PASs. Three Euler angles (α , β , and γ) describe the relative orientation, and we use the ‘ZYX’ convention herein to report these values.⁵⁴ Additional information pertaining to Euler angles has recently been summarized.⁵⁵ As magnetic shielding and QI effects on the SSNMR line shape scale differently with \mathbf{B}_0 , ^{127}I SSNMR spectra have been acquired at multiple fields, when possible, to improve the accuracy of the extracted parameters.

Spectra were simulated heuristically, without automated iteration, with special emphasis on fitting the spectral discontinuities rather than intensities. Estimation of the errors in the spectral parameters was performed by systematically altering in turn each of the parameters derived from the best fit, until the point where the simulated spectrum deviated from the experimental spectrum at one of the discontinuities by an amount comparable to the inherent point-by-point resolution of the spectrum.

To determine the \tilde{V} parameters using ^{127}I NQR data, we employed the closed-form solutions to the secular equations recently outlined by Semin,⁵⁶ which were shown to produce results identical to numerical solutions.⁵⁷

5. Quantum Chemical Calculations. GIPAW DFT computations used CASTEP-NMR (v. 4.1),^{58–61} with input files generated using Materials Studio 3.2.0.0, and either ‘ultrasoft’^{59,62} or ‘on-the-fly’ (otf) pseudopotentials. The iodine otf pseudo-

potential was obtained from Accelrys Inc. (San Diego, CA). All geometry optimizations and NMR calculations (i.e., \tilde{V} and $\tilde{\sigma}$) used the generalized gradient approximation (GGA), along with either the PBE exchange-correlation (XC) functional^{63,64} or the PW91 XC functional.^{65–69} Computed σ_{ij} values are expressed as δ_{ij} values using the following procedure: the iodine σ_{iso} for the reference (NaI) was computed using a plane wave cutoff energy (E_{cut}) of 1000 eV, a $6 \times 6 \times 6$ k -point grid, and the same XC functional as the sample of interest. Using the calculated σ_{iso} and the δ_{iso} of 226.71 ppm for NaI(s),³⁶ calculated σ_{ij} values were placed on an experimental δ scale. The E_{cut} and k -point grid used for each system are in the footnotes to Tables 3 and 4. Computed structure energies, structure references, pseudopotentials used, and additional details are in the Supporting Information, Table S2. The structural parameters used for NMR computations are in the Supporting Information, Table S3.

The $\text{SrI}_2 \cdot 6\text{H}_2\text{O}$ crystal structure has not been fully determined, but the unit cell, Sr (fully determined), and I (a , b coordinates) atomic positions have been reported.⁷⁰ It is thought that $\text{SrI}_2 \cdot 6\text{H}_2\text{O}$ is isostructural to $\text{SrCl}_2 \cdot 6\text{H}_2\text{O}$, the structure of which has been determined using neutron diffraction techniques.⁷¹ For the geometry optimization of $\text{SrI}_2 \cdot 6\text{H}_2\text{O}$, the unit cell and Sr atomic positions were frozen to the reported values. For the I, O, and H atoms, the initial guess was set to the analogous atomic positions in $\text{SrCl}_2 \cdot 6\text{H}_2\text{O}$. For $\text{BaI}_2 \cdot 2\text{H}_2\text{O}$, no structural data exist but based upon prior ^{127}I NQR data^{72,73} it is suspected to be isostructural to $\text{BaBr}_2 \cdot 2\text{H}_2\text{O}$, the structure of which is known.⁷⁴ Hence, the $\text{BaBr}_2 \cdot 2\text{H}_2\text{O}$ crystal structure was used as the starting point when optimizing the $\text{BaI}_2 \cdot 2\text{H}_2\text{O}$ crystal structure.

Results and Discussion

1. Solid-State Iodine-127 NMR and NQR Experiments.

A. Anhydrous Alkaline Earth Metal Iodides. The parameters extracted from line shape analysis of the ^{127}I SSNMR spectra for stationary (i.e., static) samples of MgI_2 , CaI_2 , SrI_2 , and BaI_2 are summarized in Table 1.

A.i. CaI_2 : Iodide Ions at High-Symmetry Lattice Positions. Iodine-127 SSNMR experiments were performed on powdered CaI_2 at $\mathbf{B}_0 = 11.75$ and 21.1 T (Figure 1). The CaI_2 crystal structure belongs to the $P\bar{3}m1$ space group and CdI_2 (2H polytype) structure class (Figure 2a).⁷⁵ There is one crystallographically unique iodide ion ($3m$ symmetry), which forms hexagonal close-packed layers with other iodide ions (Figure 2b and 2c). The local Ca–I coordination is trigonal pyramidal, with the closest iodide–iodide approach being 4.34 Å. Within

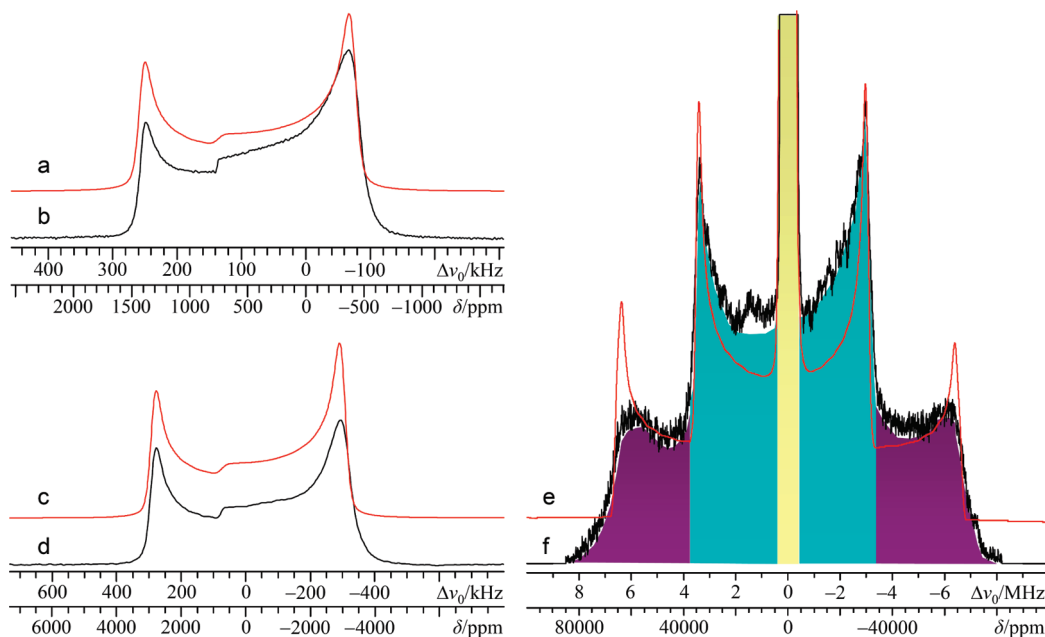


Figure 1. Analytical simulations (a, c, e), experimental static Solomon echo (b), and experimental static VOCS Hahn echo (d, f) ^{127}I SSNMR spectra of powdered CaI_2 , acquired at (b) $B_0 = 21.1$ T ($\nu_0 = 180.08$ MHz) and (d, f) $B_0 = 11.75$ T ($\nu_0 = 100.06$ MHz). The spectra in a–d correspond to the CT, while in e and f, much of the spectral region corresponds to the ST. In e and f the CT is located roughly in the region from $\Delta\nu_0 = +0.3$ to -0.4 MHz (gold), the inner ST ($m_I = \pm 3/2 \leftrightarrow \pm 1/2$) contribute most significantly from ca. $\Delta\nu_0 = +3.7$ to $+0.3$ MHz and from $\Delta\nu_0 = -0.4$ to -3.4 MHz (aqua), and the outer ST ($m_I = \pm 5/2 \leftrightarrow \pm 3/2$) contribute most significantly above $\Delta\nu_0 = +3.7$ MHz and below $\Delta\nu_0 = -3.4$ MHz (purple).

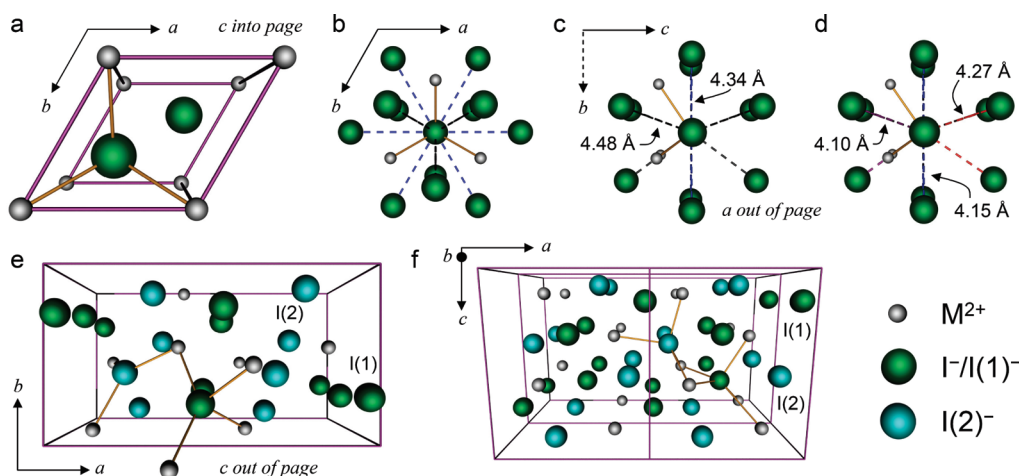


Figure 2. POV-ray renderings of the local structures for various anhydrous group 2 metal iodides. (a) CaI_2 unit cell. For the unique I, solid lines connect ions within the sum of the Ca and I van der Waals (vdW) radii (i.e., $r(\text{Ca}-\text{I}) < 4.29$ Å).^{121,122} In b and c, the local iodine environment (within 4.5 Å) for CaI_2 is shown. Six equivalent contacts (blue dashed lines) arrange hexagonally in the ab plane. A second set of equivalent contacts (black dashed lines) is related by reflection in the ab plane. (d) The iodine environment in MgI_2 is similar to CaI_2 but possesses inequivalent I–I close contacts above and below the plane defined by the hexagonal iodides (red/orange and purple dashed lines, respectively). (e) SrI_2 unit cell. Solid lines connect heteroatoms within the sum of the Sr and I vdW radii ($r(\text{Sr}-\text{I}) < 4.47$ Å). (f) BaI_2 quadruple unit cell, viewed nearly along b (10° counterclockwise rotation about the $+a$ axis). Solid lines connect heteroatoms within the sum of the Ba and I vdW radii ($r(\text{Ba}-\text{I}) < 4.66$ Å).

experimental error, the observed ^{127}I CT SSNMR signals are characteristic of axially symmetric second-order quadrupole-broadened line shapes ($\eta_Q(^{127}\text{I}) = 0.02(0.02)$). The observed ^{127}I \ddot{V} symmetry implies a 3-fold (or greater) rotational axis at the iodide,⁷⁶ in agreement with the crystal structure. Due to the strong ^{127}I CT SSNMR signal of CaI_2 , the \ddot{V} tensor was precisely characterized by collecting most of the ST at 11.75 T. The full $m_I = \pm 3/2 \leftrightarrow \pm 1/2$ ST and the high-intensity portion of the $m_I = \pm 5/2 \leftrightarrow \pm 3/2$ ST were observed (Figure 1f). While the VOCS Hahn echo spectrum in Figure 1f required the collection of 50 subspectra, each experiment lasted ca. 20 min; hence, the composite spectrum was acquired in ~ 17 h. Analytical fits of

all observed spectra establish $C_Q(^{127}\text{I})$ as 43.5(0.3) MHz and δ_{iso} as 755(10) ppm. Using analytical simulations, we estimate that $\Omega < 50$ ppm for CaI_2 , in agreement with our quantum chemical calculations (vide infra).

ii. MgI_2 : Clear Evidence of Iodine Chemical Shift Anisotropy. Iodine-127 SSNMR experiments were carried out on MgI_2 powder at $B_0 = 11.75$ and 21.1 T (Figure 3), and the observed signals were fit analytically to identical parameters (Table 1). Powder⁷⁵ and single-crystal⁷⁷ XRD data confirm that MgI_2 belongs to the same space group ($P\bar{3}m1$) and structure class as CaI_2 . In the iodide first coordination sphere, MgI_2 has three equivalent Mg–I contacts at internuclear distances of 2.9183(5)

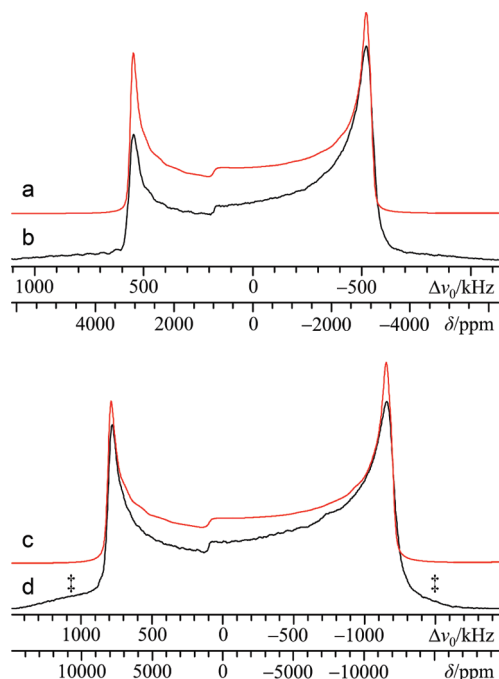


Figure 3. Analytical simulations (a, c) and experimental static VOCS Solomon echo (b, d) ^{127}I SSNMR spectra of powdered MgI_2 , acquired at (b) $B_0 = 21.1$ T and (d) $B_0 = 11.75$ T. Partially excited ST are denoted with “ \times ”.

Å. However, unlike CaI_2 , there exist numerous inequivalent I–I distances (Figure 2d) as the unique I is located at $z/c = 0.24237$, rather than at $z/c = 0.25$ as in CaI_2 .

The qualitative features of the ^{127}I SSNMR spectra of MgI_2 (Figure 3) are similar to those observed for CaI_2 . The axial \tilde{V} ($\eta_Q = 0.02(0.02)$) supports the XRD-determined local site symmetry of the iodide ions ($3m$). It is interesting to note that the measured $C_Q(^{127}\text{I})$ value of $79.8(0.5)$ MHz is nearly twice that of CaI_2 , despite the very similar crystal structures of CaI_2 and MgI_2 . This finding demonstrates the pronounced sensitivity of the ^{127}I QI to the iodide environment. To understand the origin of the drastically different \tilde{V} magnitudes in CaI_2 and MgI_2 , quantum chemical calculations were carried out (vide infra).

The measured iodine δ_{iso} of $920(50)$ ppm is significantly greater than that for CaI_2 . This can be understood by considering the Mg–I distances in the first coordination sphere of MgI_2 , which are less than the corresponding distances in CaI_2 . Relative to CaI_2 , this should lead to enhanced occupied-virtual wave function mixing in MgI_2 , which in turn results in more significant paramagnetic shielding contributions to δ .⁷⁸ Although the QI in MgI_2 contributes most of the observed ^{127}I SSNMR line width, effects due to iodine CSA in MgI_2 were observed ($\Omega = 120(80)$ ppm; Figure S1, Supporting Information). To the best of our knowledge, this represents the second reliable measurement of iodine CSA in the literature (the first for an iodide). It is roughly an order of magnitude larger than the only other precisely measured iodine Ω value, which is 18 ± 4 ppm for CsIO_4 .³⁰ We also experimentally observed that $\beta = 90(20)^\circ$, which is the first experimental observation of noncoincident iodine δ_{33} and \mathbf{V}_{33} eigenvectors. Information describing the ‘interplay’ between the \tilde{V} and δ tensors has been useful in the determination of crystallographic information, even in cases where conclusive diffraction studies are absent.⁵⁵

iii. *SrI₂: Resolution of Multiple Iodide Sites and an Approach To Determine δ_{iso} When the High-Field Approximation Is Not Obviously Valid.* Due to the very large ^{127}I QIs observed in SrI_2 (Figure 4), ^{127}I SSNMR experiments were performed at $B_0 =$

21.1 T only. The extracted ^{127}I tensor parameters are in Table 1. The SrI_2 crystal structure belongs to the $Pbca$ space group.⁷⁹ There are two inequivalent I sites, labeled as I(1) and I(2) (Figure 2e), which are present in equal proportions in the lattice. The primary differences between the two I sites are the number and geometric arrangement of the Sr^{2+} about each unique iodide: I(1) is coordinated by four Sr^{2+} , forming a distorted tetrahedron, while I(2) is coordinated by three Sr^{2+} in a distorted trigonal planar fashion. Symmetry elements do not pass through either I site; hence, both possess 1 symmetry, and the δ/\tilde{V} parameters are not symmetry restricted.

Data acquisition and analysis were carried out using conventional methods for the I(1) site; however, data collection and line shape analysis for the I(2) site required more care. For I(1), VOCS Solomon echo experiments and analytical line shape simulations (Figure 4a and 4b) of the ^{127}I SSNMR signal establish a substantial ($C_Q(^{127}\text{I}) = 105.2(0.7)$ MHz), nonaxial ($\eta_Q = 0.467(0.012)$) QI. The measured δ_{iso} value of $880(70)$ ppm lies between CaI_2 and MgI_2 ; hence, we caution against using measured iodine δ_{iso} values as direct probes of the number of heteroatomic contacts in the I first coordination sphere. For I(2), although WURST pulses were used to uniformly excite broad regions of each subspectrum, we observed moderate line shape distortions (Figure 4e) due to the finite bandwidth of the NMR probe. To the best of our knowledge, this is the first time the WURST echo pulse sequence has been used in tandem with VOCS data acquisition, although VOCS WURST-QCPMG experiments have been reported.⁸⁰ The total spectrum depicted in Figure 4e was acquired in 5 h; hence, our choice of acquisition parameters reflects a balance between uniform line shape excitation and efficient data acquisition.

For the I(2) site in SrI_2 , it was also realized that the available analytical line shape fitting software⁴⁷ may not accurately extract \tilde{V} and δ parameters. The analytical simulations assume the data are collected under high-field conditions (typically taken to be satisfied if $\nu_0 > 10\nu_Q$, where ν_Q is the quadrupolar frequency) and include the QI as perturbations to the Zeeman states to second order. We recently suggested, using simulation software that exactly combines the Zeeman and QI states (provided by Prof. A. D. Bain, McMaster University), that as a rule of thumb for $I = 5/2$, the high-field approximation is valid if $\nu_0/\nu_Q > 5$.⁸¹

Analytical fits to the observed ^{127}I SSNMR signal for the I(2) site produce the following parameters: $C_Q(^{127}\text{I}) = 213(1)$ MHz; $\eta_Q = 0.32(1)$; $\delta = 300(150)$ ppm. We intentionally neglected to specify the origin of the ‘shift’, and it is not a pure chemical shift (vide infra). To determine if the high-field approximation is valid for the I(2) site in SrI_2 at $B_0 = 21.1$ T, ν_0/ν_Q must be determined. As ^{127}I NQR experiments can be used to independently and precisely measure ν_Q , they were performed on powdered SrI_2 . The expected two signals were observed at 35.415 ($m_I = \pm 1/2 \leftrightarrow \pm 3/2$) and 62.980 ($m_I = \pm 3/2 \leftrightarrow \pm 5/2$) MHz (Figure 4, inset). The ^{127}I NQR transition frequencies establish that $C_Q = 214.0(0.1)$ MHz and $\eta_Q = 0.316(0.002)$.⁵⁶ It is important to note that these values are in quantitative agreement (i.e., within experimental error) with the \tilde{V} parameters extracted from the ^{127}I SSNMR data by way of analytical simulations, despite the low (i.e., $\nu_0 < 10\nu_Q$) ν_0/ν_Q ratio.

Since $\nu_Q = 3C_Q/[2I(2I - 1)] = 3C_Q/20$,⁸² then $\nu_Q = 32.10$ MHz and hence $\nu_0/\nu_Q \approx 5.6$. This is near our prior estimate of where the high-field approximation should no longer be valid. Using the \tilde{V} parameters determined from ^{127}I NQR experiments, a simulation using the exact QI software was generated. After adding a chemical shift ($\delta_{\text{iso}} = 720(150)$ ppm) to this simulated spectrum (Figure 4d), the agreement between it and the

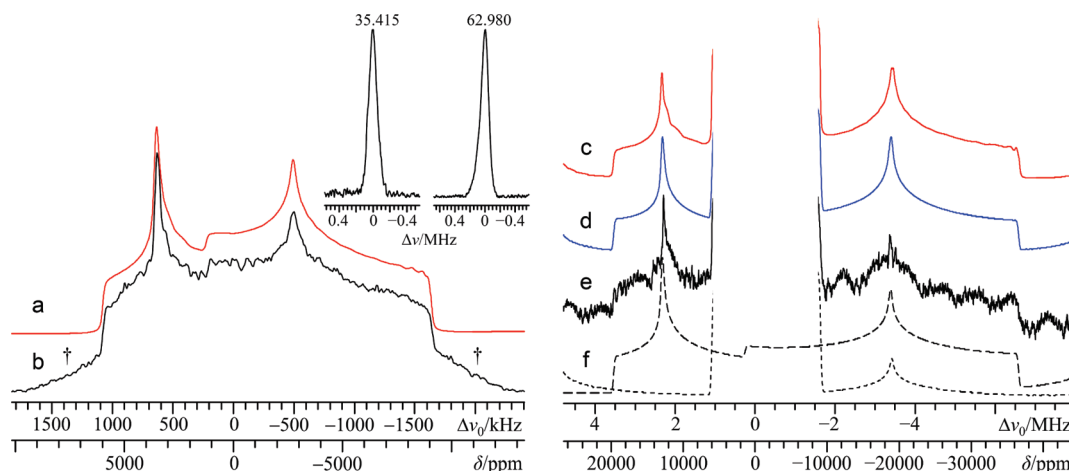


Figure 4. Analytical simulations (a, c), exact simulation (d), experimental static VOCS Solomon echo (b), and experimental static VOCS WURST echo (e) ^{127}I SSNMR spectra of powdered SrI_2 , acquired at $B_0 = 21.1$ T. In f, the two iodine sites are deconvoluted (I(1) = short dashes; I(2) = long dashes) using exact simulation software. Inclusion of the ST for I(1) is essential to reproduce the overall powder pattern. Shoulders (\dagger) in b are due primarily to the partially excited CT of I(2). Inset above a: Experimental ^{127}I NQR spectra of site I(2) in SrI_2 (left, $m_I = \pm 1/2 \leftrightarrow \pm 3/2$ transition; right, $m_I = \pm 3/2 \leftrightarrow \pm 5/2$ transition). The corresponding transition frequencies (in MHz) are listed at the top of each signal.

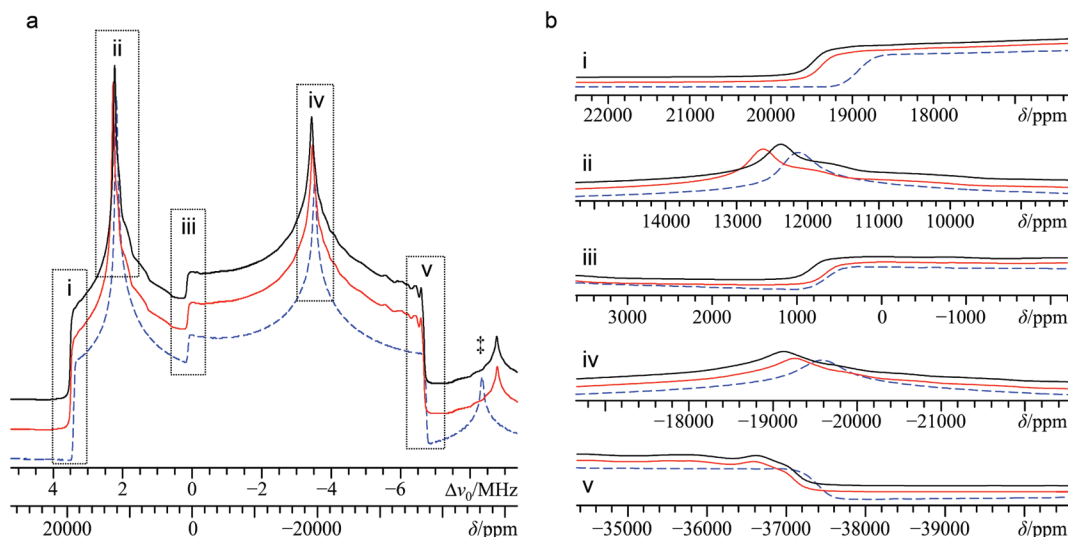


Figure 5. (a) Comparison of ^{127}I SSNMR powder patterns generated using second-order perturbation theory (solid red and black traces) with one calculated using exact theory (dashed blue trace). All are generated using the quadrupolar parameters obtained independently from a ^{127}I NQR experiment (i.e., $C_Q = 214$ MHz; $\eta_Q = 0.316$); however, chemical shift effects are ignored. Iodine CSA is included in the black trace simulation using the computed parameters in Table 3 (PBE method). Relative to the second-order perturbation theory simulations, the exact simulation is nonuniformly shifted to lower frequency. The origin of this difference is attributed to orientation-dependent higher-order QIE, as outlined in the main text. Low-frequency shoulders (\ddagger) are from ST and highlight the drastic difference in the computed position of one the ill substratities, which are affected by third-order QIE. (b) Horizontal expansions of the regions in a, as denoted by the dotted boxes. These illustrate that the incorporation of a large iodine CSA (i.e., $\Omega = 460$ ppm) generally influences the positions of the discontinuities to a lesser extent than the higher-order QIE in this case. The notable exception is the ii discontinuity, where the CSA effects are comparable to higher-order QIE. In iii, the discontinuity is affected minimally by QIE.

experimental spectrum is excellent. The ^{127}I SSNMR signal associated with the I(2) site in SrI_2 has thus provided a strict test of our earlier assertion that ν_0/ν_Q need only be greater than 5 for the high-field approximation to be valid, at least for determination of C_Q and η_Q of $I = 5/2$ nuclei.

However, considering the large difference in the ‘shifts’ obtained for the I(2) site in SrI_2 (i.e., second-order perturbation theory gives an apparent shift of 300(150) ppm, while exact theory gives 720(150) ppm), it is clear that the extraction of the correct chemical shift in this regime is *not* possible using second-order perturbation theory. Using the ^{127}I \hat{V} parameters which were determined from ^{127}I NQR experiments and neglecting chemical shift effects, we compare the line shape generated using second-order perturbation theory with one from an exact calculation (solid red and dashed blue traces, respectively, in

Figure 5a). While the pattern widths and shapes are approximately identical, it is particularly interesting to note that they are offset slightly in the frequency domain (Figure 5b). Importantly, all the horn and edge discontinuities of the exact simulation lie to lower frequency, relative to these same points generated using second-order perturbation theory. Only the central discontinuity lacks this effect (Figure 5b, iii, red and dashed blue traces) as it corresponds to crystallites where \mathbf{V}_{33} and \mathbf{B}_0 are collinear and thus is necessarily not affected by angular QI terms (vide infra).⁸³

To explain further, note that for quadrupolar nuclei with an appreciable C_Q , there is a well-known measurable shift of the SSNMR signal to lower frequency, which is known as the second-order quadrupole-induced shift (QIS). The second-order

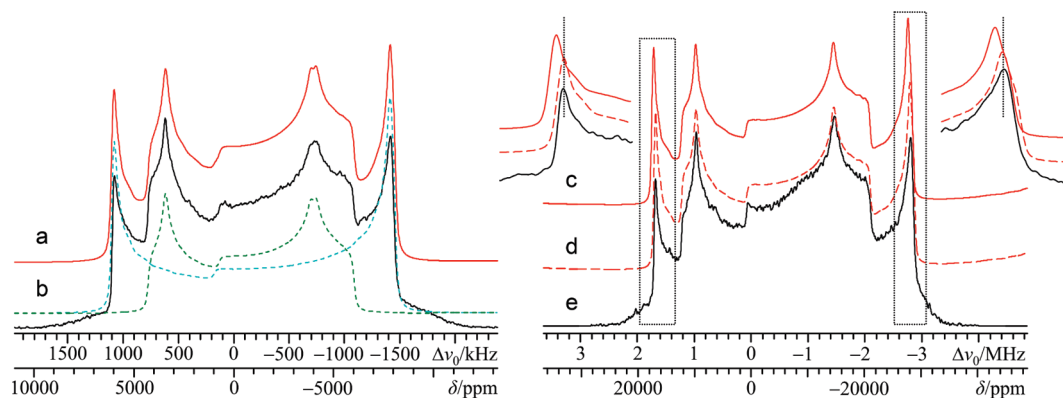


Figure 6. Analytical simulations (a, c, d), and experimental static VOCS Solomon echo (b, e) ^{127}I SSNMR spectra of powdered BaI_2 , acquired at (b) $B_0 = 21.1$ T and (e) $B_0 = 11.75$ T. A deconvolution is provided via the dotted line traces in b. The spectra inset above c correspond to the regions within the dotted boxes. They highlight the detectable deviation in the apparent chemical shift, when comparing analytical simulations at 11.75 and 21.1 T. This discrepancy is due to orientation-dependent higher-order QIE (see main text and Supporting Information Figure S5 for details). The spectra in c and d employ identical parameters, but for c, $\delta_{\text{iso}} = 1000$ ppm (i.e., the same value as in a and also shown to be correct using exact theory calculations), and for d, $\delta_{\text{iso}} = 650$ ppm.

QIS for the CT of a spin 5/2 nucleus ($\delta_{\text{QIS}}^{(2)}$, in ppm) is quantified using the following equation:⁸⁴

$$\delta_{\text{QIS}}^{(2)} = -\frac{3}{500} \left(\frac{C_Q}{\nu_0} \right)^2 \left(1 + \frac{\eta_Q^2}{3} \right) \times 10^6$$

For modest C_Q values, the chemical shift of the CT is adequately represented as $\delta_{\text{iso}} = \delta_{\text{cg}} - \delta_{\text{QIS}}^{(2)}$, where δ_{cg} is the measured position of the CT center of gravity. While third-order effects on the CT spectra for half-integer quadrupolar nuclei are zero,⁸⁵ they are nonzero for the ST and contribute to the observed line shapes in 2D experiments which involve the ST.⁸⁶ Fourth-order (and greater even-ordered) effects on the CT have not been quantified (they are thought to be nonzero); however, methods which incorporate the QI exactly exist.^{34,87–89} Returning to Figure 5, the differences in the positions of the discontinuities between the two simulated spectra can be attributed to higher-order QIE. Due to the dependence of these effects upon the crystallite orientation in a powder (i.e., the angle between \mathbf{V}_{33} and \mathbf{B}_0 for each crystallite), one is not able to assign a single value to describe this effect for the total line shape. What is clear, however, is that in this regime there are differences between the calculated positions of the discontinuities in the frequency domain (Figure 5b) and that second-order perturbation theory predicts the frequencies of these discontinuities to be too high, relative to the exact theory. Hence, one cannot use second-order perturbation theory to obtain an accurate measure of the chemical shift in this ν_0/ν_Q regime. It is also expected that as the ν_0/ν_Q ratio decreases (i.e., $\nu_0/\nu_Q < 5$ for $I = 5/2$), the ability to reliably extract \tilde{V} parameters using second-order perturbation theory will also diminish. It is precisely because this is a borderline case that we are able to properly extract C_Q and η_Q from the second-order simulation, within experimental error.

In addition, we provide an example of what impact typical CSA effects have on the line shape (black traces in Figure 5). Although we were not able to conclusively measure iodine CSA in SrI_2 , in the black simulated spectrum we set the δ values equal to those calculated in Table 3 (PBE method). Clearly, for the edge discontinuities, inclusion of even $\Omega = 460$ ppm leads to minimal differences as compared to calculations which do not include CSA (i.e., contrast the black and red solid traces in Figure 5b). Only the high-frequency horn discontinuity

(Figure 5b, trace ii) appears to be appreciably influenced by including CSA, but this lies at the limits of our measurement errors for the ca. 56 000 ppm (~ 10 MHz) broad line width for the I(2) site in SrI_2 . We additionally verified that higher-order QIE for the ^{127}I SSNMR signal of I(1) in SrI_2 are below our measurement errors (Supporting Information, Figure S2). This is expected, as the fourth-order term (i.e., the leading term not included in second-order perturbation theory) that would influence the CT should possess roughly a $(C_Q/\nu_0)^4$ dependence.

iv. BaI_2 : Resolution of Iodide Sites Possessing Similar QI and Observation of higher-order QIE When the High-Field Approximation Is Not Clearly Valid at a Standard Field. Iodine- ^{127}I SSNMR experiments were carried out on powdered BaI_2 at $B_0 = 11.75$ and 21.1 T, and the measured parameters are in Table 1. All observed ^{127}I SSNMR signals were fit to identical parameters using analytical simulations, except for the chemical shift of site I(2), as analytical simulations at the two applied fields produced two different apparent chemical shift values for this site. Exact simulations were performed and confirm the δ_{iso} values measured at $B_0 = 21.1$ T (Supporting Information, Figure S3). BaI_2 belongs to the $Pnma$ space group and possesses two unique I^- within the crystal lattice, which are labeled I(1) and I(2), as in Figure 2f.⁹⁰ Both sites possess m symmetry, which constrains the potential Euler angle values. The primary difference between the two I^- sites in BaI_2 is that I(1) is coordinated by 5 Ba^{2+} ions while I(2) is coordinated by 4 Ba^{2+} ions.

Inspection of the ^{127}I SSNMR spectra of BaI_2 (Figure 6b and 6e) clearly reveals that the \tilde{V} magnitudes for both I sites are similar, as the corresponding ^{127}I SSNMR signal line widths are comparable. Relative to SrI_2 , BaI_2 represents a more stringent test of the resolving power of ^{127}I SSNMR. The $C_Q(^{127}\text{I})$ value for the 5-coordinate I(1) site is slightly smaller than that for the 4-coordinate I(2) site (i.e., 96.2(0.8) vs 120.9(0.2) MHz). While the ^{127}I EFG tensor at the I(1) site is not axially symmetric ($\eta_Q = 0.175(0.015)$), the \tilde{V} at the I(2) site is observed to be axial ($\eta_Q = 0.015(0.015)$). The \tilde{V} is not constrained here to be axial by the lattice symmetry. Likewise, quantum chemical calculations using the crystal structure do not predict an axial EFG tensor (vide infra) for either site, in disagreement with our ^{127}I SSNMR data for I(2). For the I(2) site, however, ^{127}I NQR experiments were performed and confirm the \tilde{V} parameters determined using analytical fits to the ^{127}I SSNMR signal.

TABLE 2: Experimental ^{127}I EFG and Chemical Shift Tensor Parameters: Group 2 Metal Iodide Hydrates^a

compound	$ C_Q(^{127}\text{I}) /\text{MHz}$	η_Q	$\delta_{\text{iso}}/\text{ppm}$	Ω/ppm	κ	α/deg	β/deg	γ/deg	notes
$\text{BaI}_2 \cdot 2\text{H}_2\text{O}$	53.8(0.3)	0.53(0.01)	630(20)	60(15)	>0.5	45(15)	45(15)	—	$T = 295\text{ K}$
	52.4(0.3)	0.56(0.01)	630	60	>0.5	45	45	—	$T \approx 243\text{ K}$
	53.7(0.3)	0.532(0.004)	—	—	—	—	—	—	ref 73
$\text{SrI}_2 \cdot 6\text{H}_2\text{O}$	133.6(0.1) ^b	<0.01	440(25) ^c	—	—	—	—	—	NQR: $\nu_1 = 20.034(0.015)$; $\nu_2 = 40.068(0.015)$ ^d

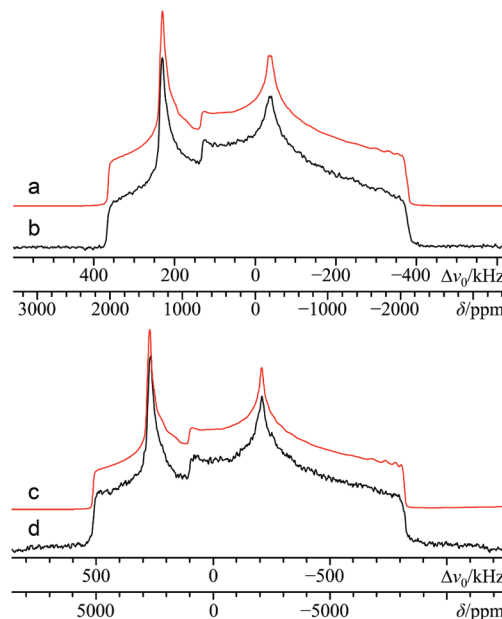
^a Error bounds are in parentheses. ^b Established with the aid of ^{127}I NQR experiments. ^c Established with the aid of exact simulation software.^d All ^{127}I NQR frequencies are in MHz.

Definitive evidence of iodine CSA is present in the ^{127}I SSNMR spectrum of site I(1), due to the characteristic broadening of the low-frequency ‘horn’ discontinuity, which often results from β deviating from either 0° or 90° ($\beta = 45(20)^\circ$; see Supporting Information, Figure S4). The measured iodine Ω value for the I(1) site is the largest reported ($\Omega = 300(100)$ ppm). While analytical line shape simulations at both \mathbf{B}_0 lead to the same δ_{iso} value for the I(1) site, this is not the case for the I(2) site, which possesses the larger $C_Q(^{127}\text{I})$ value. An analytical simulation of the I(2) signal acquired at $\mathbf{B}_0 = 21.1\text{ T}$ leads to $\delta_{\text{iso}} = 1000(80)$ ppm, while the same simulation method using the signal acquired at $\mathbf{B}_0 = 11.75\text{ T}$ produces an apparent shift of 650 ppm. As with the ^{127}I SSNMR spectrum for site I(2) in SrI_2 , this is clear evidence of higher-order QIE for the I(2) site at 11.75 T only. As with site I(2) in SrI_2 , the higher-order QIE is manifested in the extracted chemical shift values, rather than in the \tilde{V} parameters. It is interesting that the QIE are only detectable at the lower applied field and only for the site with the larger C_Q value. This is expected, as higher-order QIE are anticipated for lower ν_0/ν_Q ratios. Of course, one may easily rule out CSA effects as the source of the seemingly field-dependent chemical shift for site I(2) in BaI_2 , as CSA effects scale directly with the applied field, rather than inversely.

B. Hydrated Alkaline Earth Metal Iodides: The Effects of Hydration upon Iodine SSNMR Parameters. We carried out ^{127}I SSNMR experiments on two group 2 metal iodide hydrates to observe if there is an effect on the ^{127}I SSNMR parameters as a result of hydration. Previously, $^{35/37}\text{Cl}$ and $^{79/81}\text{Br}$ SSNMR experiments on several $\text{MX}_2 \cdot n\text{H}_2\text{O}$ systems ($\text{M} = \text{group 2 metal}$, $\text{X} = \text{Cl or Br}$, $n = 2, 4, 6$) have established that a decrease in the halogen chemical shift correlates with an increasing degree of hydration.^{22,26} It has also been observed in many cases (but not always) that an increase in hydration leads to a decrease in the value of the halogen C_Q . The newly observed NMR parameters are summarized in Table 2.

B.i. $\text{BaI}_2 \cdot 2\text{H}_2\text{O}$. The crystal structure of $\text{BaI}_2 \cdot 2\text{H}_2\text{O}$ has not been determined; however, using ^{127}I and $^{135/137}\text{Ba}$ NQR data, it has been suggested that $\text{BaI}_2 \cdot 2\text{H}_2\text{O}$ is isostructural to $\text{BaBr}_2 \cdot 2\text{H}_2\text{O}$.^{72,73} We will make further comments on their isostructural nature and propose a solid-state structure for $\text{BaI}_2 \cdot 2\text{H}_2\text{O}$ in the quantum chemical calculations section (vide infra).

Using powdered $\text{BaI}_2 \cdot 2\text{H}_2\text{O}$, identical ^{127}I EFG and CS tensor parameters were extracted from the ^{127}I SSNMR spectra measured at $\mathbf{B}_0 = 11.75$ and 21.1 T (Figure 7). It is interesting to note that grinding the sample, even under an inert atmosphere, creates a second phase (Figures S6 and S7, Supporting Information). The \tilde{V} parameters measured using the ^{127}I SSNMR line shapes in Figure 7 (i.e., $C_Q(^{127}\text{I}) = 53.8(0.3)\text{ MHz}$; $\eta_Q = 0.53(0.01)$) match quantitatively with those measured using ^{127}I NQR.⁷² Proton decoupling was essential to resolve the fine spectral detail at 21.1 T (Figure S6, Supporting Information), which allows us to quantify \tilde{V} and δ tensor noncoincidence. We also confirmed, using variable temperature ^{127}I SSNMR

**Figure 7.** Analytical simulations (a, c), experimental static VOCS $^{127}\text{I}\{^1\text{H}\}$ Solomon echo (b), and ^{127}I Hahn echo (d) SSNMR spectra of powdered $\text{BaI}_2 \cdot 2\text{H}_2\text{O}$, acquired at (b) $\mathbf{B}_0 = 21.1\text{ T}$ and (d) $\mathbf{B}_0 = 11.75\text{ T}$.

experiments (Figure S7, Supporting Information), that the temperature dependence of the \tilde{V} parameters is identical to that observed using ^{127}I NQR. As expected, the iodine chemical shift ($\delta_{\text{iso}} = 630(20)$ ppm) is low relative to the anhydrous compounds discussed earlier.

ii. $\text{SrI}_2 \cdot 6\text{H}_2\text{O}$. While the unit cell and select heavy atom positions of $\text{SrI}_2 \cdot 6\text{H}_2\text{O}$ were determined many years ago,⁷⁰ the full crystal structure remains unpublished. It is currently accepted that $\text{SrI}_2 \cdot 6\text{H}_2\text{O}$ is isostructural with $\text{SrCl}_2 \cdot 6\text{H}_2\text{O}$.⁷¹ Iodine- ^{127}I SSNMR experiments were carried out using powdered $\text{SrI}_2 \cdot 6\text{H}_2\text{O}$ at $\mathbf{B}_0 = 21.1\text{ T}$ (Figure 8), and the measured parameters may be found in Table 2. The observed ^{127}I SSNMR signal provides evidence for a single I environment, which is within an axial EFG ($\eta_Q = 0$). Using analytical simulation software, the measured apparent shift ($\delta = 390(25)$ ppm) is shielded relative to all the other compounds studied, consistent with the expected trend for halogen chemical shifts upon increasing hydration.

As the iodine QI in $\text{SrI}_2 \cdot 6\text{H}_2\text{O}$ is rather significant ($C_Q(^{127}\text{I}) = 133.6(0.1)\text{ MHz}$), ^{127}I NQR experiments were also performed for this compound and confirmed the \tilde{V} parameters extracted from modeling the ^{127}I SSNMR spectrum. In addition, since the ^{127}I SSNMR spectrum possessed very sharply defined ‘horn’ discontinuities, we carried out exact simulations for this compound in the hopes of finding higher-order QIE. Using exact theory, we again confirm the above $C_Q(^{127}\text{I})$ and η_Q but also found that $\delta_{\text{iso}} = 440(25)$ ppm (Figure S8, Supporting Informa-

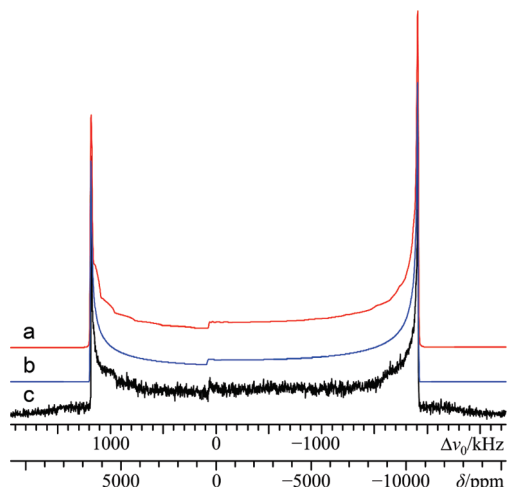


Figure 8. Analytical simulation (a), exact simulation (b), and experimental static VOCS Solomon echo (c) ^{127}I SSNMR spectra of powdered $\text{SrI}_2 \cdot 6\text{H}_2\text{O}$, acquired at $B_0 = 21.1$ T.

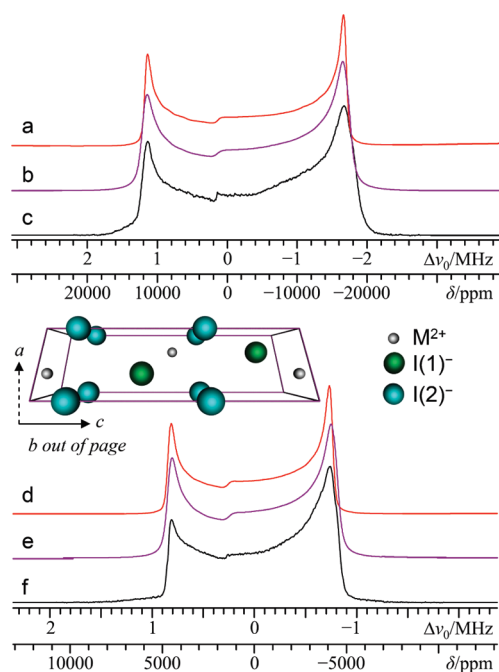


Figure 9. One-site analytical simulations (a, d), two-site analytical simulations (b, e) and experimental (c, f) static Solomon echo ^{127}I SSNMR spectra of powdered CdI_2 (4H), acquired at $B_0 = 11.75$ T (c) and $B_0 = 21.1$ T (f). Inset: CdI_2 (4H) unit cell, as viewed along the $+b$ axis.

tion), which is evidence of higher-order QIE for this compound. We were unable to conclusively measure iodine CSA in $\text{SrI}_2 \cdot 6\text{H}_2\text{O}$.

C. CdI_2 (4H): Application of Iodine-127 SSNMR to a Semiconducting Material. Cadmium iodide is a polytypic semiconducting material.⁹¹ In general, polytypic materials result from one-dimensional disorder due to stacking faults. The common polytype of CdI_2 , denoted as 4H, belongs to the $P6_3mc$ space group and possesses a stacking fault along the c axis, which doubles the c value relative to the CdI_2 (2H) polytype.⁹² There are two unique iodide sites per unit cell (Figure 9, inset). Both ^{127}I NQR^{93–95} and ^{113}Cd NMR^{96–98} data exist for CdI_2 (4H).

Iodine-127 SSNMR experiments were performed at 11.75 and 21.1 T on a powdered sample of CdI_2 (4H) (Table 1). The observed ^{127}I SSNMR signals at both fields exhibit very broad ‘horn’ discontinuities (Figure 9); hence, it is not possible to

resolve the two expected I sites in this material. According to prior ^{127}I NQR data, the ν_Q values for the two sites differ by only 2%,⁹⁴ thus, the inability to resolve the sites using ^{127}I SSNMR is not surprising. Using a one-site model (Figure 9a and 9d), a moderately large ($C_Q(^{127}\text{I}) = 95.7(1.0)$ MHz), axial QI is observed, in very good agreement with prior ^{127}I NQR measurements. The breadth of the horn discontinuities hints at a second iodine site, which has a similar EFG tensor (see Figure 9b and 9e for fits using a two-site model). Although CSA was neglected in our line shape simulations, the observed $\delta_{\text{iso}} = 1450(100)$ ppm (one-site model) is very significantly deshielded relative to the other compounds studied. This effect could be expected, as semiconducting materials have relatively reduced HOMO–LUMO gaps (Δ_{HL}). According to Ramsey’s model of magnetic shielding,^{99–101} paramagnetic shielding contributions are enhanced by a smaller Δ_{HL} , which generally leads to reduced nuclear shielding (i.e., a more positive chemical shift).

D. Discussion of Halogen SSNMR Parameters Across the Group 2 Metal Halides.

i. Nuclear Quadrupole Coupling Constants. Earlier, it was observed that the group 2 metal chloride and bromide hydrates nearly always possess smaller $C_Q(\text{X})$ values when compared to their anhydrous analogs.^{22,26} This appears to also hold true for the group 2 iodides. As each quadrupolar halogen nucleus possesses a unique Q , direct comparisons of interhalogen $C_Q(\text{X})$ values should not be made. Clearly, when one compares similar systems, it is typically observed that $C_Q(^{127}\text{I}) \gg C_Q(^{79}\text{Br}) > C_Q(^{81}\text{Br}) \gg C_Q(^{35}\text{Cl}) > C_Q(^{37}\text{Cl})$.

It has been demonstrated that a linear relationship exists when C_Q is plotted against $Q(1 - \gamma_\infty)/V$, where γ_∞ is the Sternheimer antishielding factor^{102–104} for each atom and V is the unit cell volume for a given compound.¹⁰⁵ Within the group 2 metal halide compounds that have been studied, many isostructural compounds are known (i.e., $\text{MgBr}_2/\text{MgI}_2$, $\text{MgCl}_2 \cdot 6\text{H}_2\text{O}/\text{MgBr}_2 \cdot 6\text{H}_2\text{O}$, $\text{CaCl}_2/\text{CaBr}_2$, $\text{BaCl}_2/\text{BaBr}_2/\text{BaI}_2$, $\text{SrCl}_2 \cdot 6\text{H}_2\text{O}/\text{SrBr}_2 \cdot 6\text{H}_2\text{O}$), while others are suspected (i.e., $\text{BaBr}_2 \cdot 2\text{H}_2\text{O}/\text{BaI}_2 \cdot 2\text{H}_2\text{O}$, $\text{Sr}(\text{Cl}/\text{Br})_2 \cdot 6\text{H}_2\text{O}/\text{SrI}_2 \cdot 6\text{H}_2\text{O}$). From the known isostructural series where sufficient data exist, the linear relationship between C_Q and $Q(1 - \gamma_\infty)/V$ is again observed (Supporting Information, Figure S9). Where data are sparse, observed C_Q ratios (e.g., $C_Q(^{81}\text{Br})/C_Q(^{35}\text{Cl})$ in $\text{CaBr}_2/\text{CaCl}_2$) should closely agree with the corresponding calculated $Q(1 - \gamma_\infty)/V$ ratios.²⁶ Input data for these computations, as well as the ratios, are summarized in Tables S4 and S5 of the Supporting Information. Overall, there is fair agreement between C_Q and $Q(1 - \gamma_\infty)/V$ ratios (average difference = 20.1%).

On the basis of the above results, it is likely that the relationship between C_Q and $Q(1 - \gamma_\infty)/V$ could help confirm whether two compounds are isostructural. We carried out simple calculations using literature values (see Table S4, Supporting Information) for the relevant parameters (except the unit cell volume for $\text{BaI}_2 \cdot 2\text{H}_2\text{O}$, which was computationally optimized (vide infra)) to establish if $\text{Sr}(\text{Cl}/\text{Br})_2 \cdot 6\text{H}_2\text{O}$ and $\text{BaBr}_2 \cdot 2\text{H}_2\text{O}$ are isostructural to $\text{SrI}_2 \cdot 6\text{H}_2\text{O}$ and $\text{BaI}_2 \cdot 2\text{H}_2\text{O}$, respectively. By plotting C_Q versus $Q(1 - \gamma_\infty)/V$ for the suspected isostructural series of $\text{SrX}_2 \cdot 6\text{H}_2\text{O}$ ($\text{X} = \text{Cl}, \text{Br}, \text{I}$), a linear relationship is observed (Supporting Information, Figure S10). This finding adds support to the argument that $\text{SrI}_2 \cdot 6\text{H}_2\text{O}$ belongs to this isostructural series. Similarly, for $\text{BaBr}_2 \cdot 2\text{H}_2\text{O}$ and $\text{BaI}_2 \cdot 2\text{H}_2\text{O}$, the $C_Q(^{127}\text{I})/C_Q(^{79}\text{Br})$ ratio is 6.16 whereas the calculated $(Q(^{127}\text{I})[1 - \gamma_\infty(\text{I})]/V_{\text{I}})/(Q(^{79}\text{Br})[1 - \gamma_\infty(\text{Br})]/V_{\text{Br}})$ ratio is 3.71 (% difference = 49.6%). The $C_Q/[Q(1 - \gamma_\infty)/V]$ relationship therefore cannot confirm the postulated isostructural nature

between $\text{BaBr}_2 \cdot 2\text{H}_2\text{O}$ and $\text{BaI}_2 \cdot 2\text{H}_2\text{O}$; rather, it hints that they are not exactly isostructural.

ii. Halogen Chemical Shifts. If the halogen chemical shift values of the group 2 metal halides can be understood in a similar fashion as the group 1 metal halides, then it is the orbital overlap between the halogen ion and both its nearest and next-nearest neighbors which largely determines the observed chemical shifts.^{106,107} As with the group 2 metal chlorides and bromides, a significant decrease in the observed halogen chemical shift results upon increasing the degree of hydration for the group 2 metal iodides. Structurally, it is also generally seen that increasing hydration increases the average internuclear metal–halogen first-coordination sphere distance ($\overline{r(\text{M}-\text{X})}$), and/or decreases the number of M^{2+} species in the halogen first-coordination sphere. Neglecting polarization effects, an increase in $\overline{r(\text{M}-\text{X})}$ must lead to reduced $\text{M}-\text{X}$ orbital overlap, which in turn decreases paramagnetic shielding contributions to δ .⁷⁸ As paramagnetic shielding normally corresponds to positive chemical shifts, a reduced contribution to this shielding mechanism would lead to reduced chemical shifts, as typically observed.

It has also been observed that there is some overlap in the halogen chemical shift regions corresponding to anhydrous, dihydrate, and hexahydrate compounds for the chlorides,²² while this overlap is not observed for the heavier halogens. The reason for the decreased overlap for the heavier nuclides may be rationalized using the arguments of Jameson and Gutowsky: they noted that the chemical shift ranges for the main group elements correlate with the value of $\langle 1/r^3 \rangle_{np}$, which is the average value of $1/r^3$ over the valence p electrons for a free atom.¹⁰⁸ As diamagnetic shielding is strongly dependent upon the core electrons,⁷⁸ its value is largely invariant with respect to the chemical environment. Hence, the observed variation in the δ_{iso} ranges across the main group nuclides is largely due to differences in paramagnetic shielding. According to a recent review of the quadrupolar halogen nuclei, the total known chlorine, bromine, and iodine δ_{iso} ranges are roughly 1100, 2700, and 4050 ppm, respectively.³⁶ Corresponding δ_{iso} ranges for the group 2 metal chlorides, bromides, and iodides (including hydrates) are ca. 185, 420, and 560 ppm.^{22,26,27} When these ranges are plotted as a function of $\langle a_0^3/r^3 \rangle_{np}$ (a_0 is the atomic Bohr radius), linear relationships with high correlation coefficients (both $R^2 > 0.997$) are observed (Figure 10). According to the above relationship, the chemical shift ranges for particular groupings of compounds should exhibit less overlap for bromine and iodine, relative to chlorine, as observed.

2. Quantum Chemical Calculations. GIPAW DFT⁵⁸ quantum chemical calculations have recently proven to be accurate for the calculation of NMR parameters for a variety of nuclei in inorganic systems.^{22,26,109–115} As crystal structures exist for all the anhydrous compounds studied here, GIPAW DFT was used to calculate energies and δ/\dot{V} for these compounds. Computed energies and the crystal structures used can be found in the Supporting Information, Tables S2 and S3, while the calculated iodine SSNMR parameters are in Tables 3 and 4.

A. Structure Proposals for $\text{BaI}_2 \cdot 2\text{H}_2\text{O}$ and $\text{SrI}_2 \cdot 6\text{H}_2\text{O}$. As noted earlier, fully refined structural data are not available for $\text{SrI}_2 \cdot 6\text{H}_2\text{O}$ and structural data do not exist for $\text{BaI}_2 \cdot 2\text{H}_2\text{O}$. Earlier studies have assumed that $\text{SrI}_2 \cdot 6\text{H}_2\text{O}$ and $\text{BaI}_2 \cdot 2\text{H}_2\text{O}$ are isostructural to their analogous metal bromide hydrates.^{70,72,73} GIPAW DFT was successfully used to generate optimized structures for both, the coordinates of which can be found in the Supporting Information, Table S3. These optimized structures were used for subsequent NMR tensor calculations.

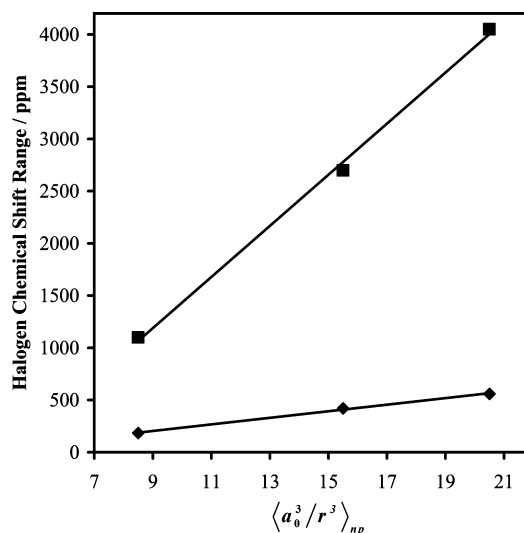


Figure 10. Plot of the observed halogen chemical shift ranges versus $\langle a_0^3/r^3 \rangle_{np}$ for all compounds (■ series) and for group 2 metal halides (◆ series). The lines of best fit are as follows: ◆ series, $y = 31.399x - 77.42$, $R^2 = 0.9976$; ■ series, $y = 244.72x - 1013.4$, $R^2 = 0.9978$. All $\langle a_0^3/r^3 \rangle_{np}$ values are from ref 123.

B. Calculated Iodine δ and \dot{V} Magnitudes, Symmetries, and Orientations. As with the group 2 chlorides and bromides studied earlier,^{22,26} the GIPAW DFT method reproduces the experimental halogen SSNMR parameters reasonably well in several cases (Figure 11). Calculated and experimental $C_Q(^{127}\text{I})$ values are in very good to excellent agreement (rmsd = 13.8 MHz, excluding the $\text{SrI}_2 \cdot 6\text{H}_2\text{O}$ datum) in most cases (Figure 11a), although the computed magnitudes are typically slightly greater than those observed (rather notably so for the optimized hydrate structures). Quantitative agreement between calculated and experimental η_Q values (Figure 11b) is observed in all cases where the local site symmetry constrains the EFG to be axial (i.e., MgI_2 , CaI_2 , CdI_2 (4H), and $\text{SrI}_2 \cdot 6\text{H}_2\text{O}$) and in select cases when the EFG is not constrained to be axial (i.e., SrI_2 , site I(2) and BaI_2 , site I(1)). On the basis of the very good agreement between the experimental and the computed values for C_Q and η_Q , it can be stated that relativistic contributions to the \dot{V} appear to be minimal in these systems. Calculated δ_{iso} values are typically overestimated relative to experiment (Figure 11c) but reproduce the observed trend in δ_{iso} (i.e., $\delta_{\text{iso}}(\text{CdI}_2 \text{ (4H)}) \gg \delta_{\text{iso}}(\text{MI}_2) > \delta_{\text{iso}}(\text{BaI}_2 \cdot 2\text{H}_2\text{O}) > \delta_{\text{iso}}(\text{SrI}_2 \cdot 6\text{H}_2\text{O})$).

For the remaining parameters, experimental data exist for only three compounds; hence, definitive conclusions cannot be made. The \dot{V} and δ eigenvectors have been calculated and are presented in their respective crystal frames in Figures S11–S17 of the Supporting Information, while normalized eigenvector components are in Table S8, Supporting Information. As with the group 2 metal bromides,²⁶ the tensor eigenvectors often (but not in general) point toward a nearby ion.

C. Understanding the Dramatically Different $C_Q(^{127}\text{I})$ Values for MgI_2 and CaI_2 . Here we rationalize the substantial difference in the observed $C_Q(^{127}\text{I})$ values for MgI_2 and CaI_2 , two compounds which were long considered to be isostructural. In 2003, it was revealed that while both belong to the $P\bar{3}m1$ space group and place the halide anions at 2d Wyckoff sites (i.e., $x/a = 0$, $y/b = 0$, $z/c = u$, where u is variable), they do possess slightly different u values ($u = 0.25$ and 0.24237 for CaI_2 and MgI_2 , respectively).⁷⁷ As demonstrated above for several isostructural compounds, if MgI_2 and CaI_2 were isostructural, they should possess similar $C_Q(^{127}\text{I})$ values, likely scaled by the ratio of their unit cell volumes. As the halogen u

TABLE 3: GIPAW DFT-Computed ^{127}I EFG and Chemical Shift Tensor Parameters: Anhydrous Metal Iodides^a

functional	site label	$C_Q(^{127}\text{I})/\text{MHz}$	η_Q	Ω/ppm	κ	$\delta_{\text{iso}}/\text{ppm}$	α/deg	β/deg	γ/deg
MgI₂									
PBE	—	80.97	0.000	145.1	−1.00	1189.8	89.3	90.0	0.0
PW91	—	81.42	0.000	144.0	−1.00	1192.8	89.3	90.0	0.0
CaI₂									
PBE	—	42.21	0.000	5.8	1.00	1076.8	90.0	0.0	90.0
PW91	—	43.19	0.000	6.0	1.00	1099.6	90.0	0.0	90.0
SrI₂									
PBE	I(1)	−107.92	0.326	221.3	0.39	1034.1	138.7	36.3	259.1
	I(2)	231.34	0.321	460.5	0.63	947.6	104.6	89.8	333.7
PW91	I(1)	−108.59	0.325	217.0	0.40	1043.5	137.1	35.5	257.7
	I(2)	232.83	0.319	458.4	0.63	953.9	104.2	89.7	333.2
BaI₂									
PBE	I(1)	84.60	0.176	493.8	−0.63	889.4	0.0	47.1	180.0
	I(2)	−151.19	0.078	239.4	0.48	1230.6	180.0	36.4	180.0
PW91	I(1)	84.73	0.180	496.4	−0.63	906.0	0.0	47.2	180.0
	I(2)	−151.86	0.077	242.6	0.49	1250.7	180.0	36.5	180.0
CdI₂ (4H)									
PBE	I(1)	90.09	0.000	171.8	−0.99	2078.2	273.1	90.0	180.0
	I(2)	93.30	0.000	428.0	−1.00	1937.5	273.0	90.0	180.0
PW91	I(1)	92.05	0.000	181.7	−0.99	2169.6	273.0	90.0	180.0
	I(2)	95.37	0.000	449.1	−1.00	2023.8	273.0	90.0	180.0

^a Parameter definitions are in the main text. ^b $Q(^{127}\text{I}) = -6.96 \times 10^{-29} \text{ m}^2$.³¹ To convert V_{33} into frequency units, a conversion factor of $-163.535487 \text{ MHz/au}$ was used, and the unit EFG (in au) equals $9.71736166 \times 10^{21} \text{ J C}^{-1} \text{ m}^{-2}$. MgI₂ calculations used $E_{\text{cut}} = 1000 \text{ eV}$ and a $9 \times 9 \times 6$ k -point grid; CaI₂ calculations used $E_{\text{cut}} = 1200 \text{ eV}$ and a $9 \times 9 \times 6$ k -point grid; SrI₂ calculations used $E_{\text{cut}} = 550 \text{ eV}$ and a $2 \times 4 \times 4$ k -point grid; BaI₂ calculations used $E_{\text{cut}} = 600 \text{ eV}$ and a $4 \times 6 \times 3$ k -point grid; CdI₂ (4H) calculations used $E_{\text{cut}} = 1000 \text{ eV}$ and a $9 \times 9 \times 2$ k -point grid. For further computational details, see the Supporting Information: Tables S2, S3, and S6.

TABLE 4: GIPAW DFT-Computed ^{127}I EFG and Chemical Shift Tensor Parameters: Group 2 Metal Iodide Hydrates

functional	$C_Q(^{127}\text{I})/\text{MHz}$	η_Q	Ω/ppm	κ	$\delta_{\text{iso}}/\text{ppm}$	α/deg	β/deg	γ/deg
SrI₂·6H₂O^a								
PBE	191.37	0.000	14.3	−0.99	352.9	357.7	90.0	180.1
PW91	191.17	0.000	14.9	−0.99	362.9	358.8	90.0	180.1
BaI₂·2H₂O^b								
PBE	65.86	0.408	82.5	−0.38	663.6	250.4	86.4	325.0
PW91	66.67	0.429	84.1	−0.36	681.0	251.7	86.4	324.7

^a Geometry optimization used $E_{\text{cut}} = 700 \text{ eV}$, while NMR parameter calculations used $E_{\text{cut}} = 800 \text{ eV}$. All calculations used a $5 \times 5 \times 8$ k -point grid. ^b Geometry optimization used $E_{\text{cut}} = 450 \text{ eV}$, while NMR parameter calculations used $E_{\text{cut}} = 650 \text{ eV}$. All calculations used a $2 \times 3 \times 3$ k -point grid. For further computational details, see the Supporting Information: Tables S2, S3, and S7.

value is the only clear difference between these two structures, we performed a quantum chemical study where u for each of MgI₂ and CaI₂ was incremented. A summary of the $C_Q(^{127}\text{I})$ and system energy variation as a result of small displacements (i.e., $\pm 0.07 \text{ \AA}$) from the crystallographic positions parallel to the c crystal axis (i.e., Δc) is provided in Figure 12. It is immediately clear that very subtle alterations in u result in a substantial augmentation of the calculated $C_Q(^{127}\text{I})$ value for both compounds. For MgI₂, the total variation in the calculated $C_Q(^{127}\text{I})$ values ranges from 140 to 19.6 MHz (Figure 12a). Similar behavior is seen for CaI₂ (Figure 12b). In light of the sensitivity of $C_Q(^{127}\text{I})$ to structure, it is remarkable that the values calculated for CaI₂ and MgI₂ using the known crystal structures agree nearly quantitatively with experiment. It is clear that ^{127}I SSNMR observations, when coupled with GIPAW DFT calculations, may be applied to further refine crystal structures of inorganic systems, as previously shown for other nuclides.^{27,55} This may also explain why our computed $C_Q(^{127}\text{I})$ values for the optimized BaI₂·2H₂O and SrI₂·6H₂O crystal structures differ

more from the observed values, relative to the cases where XRD or neutron diffraction structures were available.

Conclusions

Iodine-127 SSNMR has been established as a useful tool for probing the environment of iodide ions in inorganic solids. The pronounced sensitivity of the ^{127}I NMR interaction tensors to local symmetry elements and structure has been demonstrated and holds a potential application in crystallographic structure refinement. As ultrahigh magnetic fields become increasingly accessible, it is clear that SSNMR experiments on ‘exotic’ quadrupolar nuclei like ^{127}I will be able to provide useful information regarding the structure and electronic environment about iodide ions. We find that multiple field data acquisition can be used to aid in the extraction of iodine CSA data; however, due to the extreme CT signal breadth in several of these systems (up to 10 MHz/56 000 ppm), one is not always able to perform the experiments at lower field due to sensitivity issues.

We observed orientation-dependent higher-order quadrupole-induced effects using NMR spectroscopy in tandem with independent NQR measurements and exact QI simulation software. We have shown that these effects generally shift the powder pattern to lower frequency, relative to what would be expected using second-order perturbation theory. Hence, exact QI models are required to correctly extract the chemical shift in this regime. Consideration of these effects will be essential for the correct interpretation of SSNMR spectra for a variety of quadrupolar nuclei which experience a large quadrupolar interaction.

A number of pertinent trends have been observed. Using C_Q values, halogen SSNMR spectroscopy is shown to be useful in confirming isostructural series, and its predictive power in this regard is illustrated using the $\text{SrX}_2 \cdot 6\text{H}_2\text{O}$ ($\text{X} = \text{Cl}, \text{Br}, \text{I}$) series. There is a clear trend in decreasing halogen δ_{iso} values as the hydration level of the group 2 metal halide structure is increased,

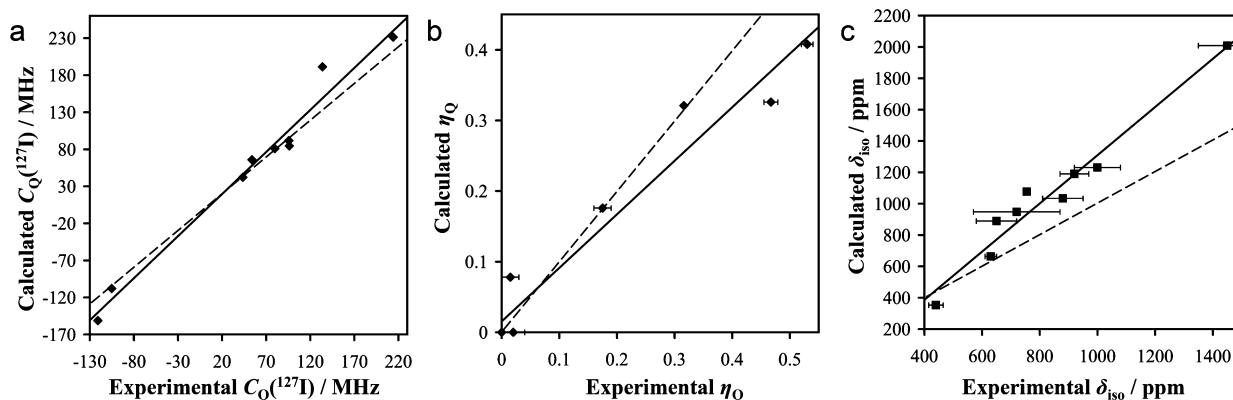


Figure 11. Plots of GIPAW DFT results versus experimental values for (a) $C_Q(^{127}\text{I})$, (b) η_Q , and (c) δ_{iso} . Experimental data are taken from Tables 1 and 2, while the calculated data are from Tables 3 and 4. The calculated results used the PBE XC functional. Solid lines are of best linear fit, while dashed lines represent an ideal fit (i.e., $y = x$). The lines of best fit are as follows: (a) $C_Q(^{127}\text{I,calcd}) = 1.135(C_Q(^{127}\text{I,exp})) - 3.127$, $R^2 = 0.9755$; (b) $\eta_Q(\text{calcd}) = 0.758(\eta_Q(\text{exp})) + 0.016$, $R^2 = 0.9457$; (c) $\delta_{\text{iso}}(\text{calcd}) = 1.537(\delta_{\text{iso}}(\text{exp})) - 227.48$, $R^2 = 0.9581$.

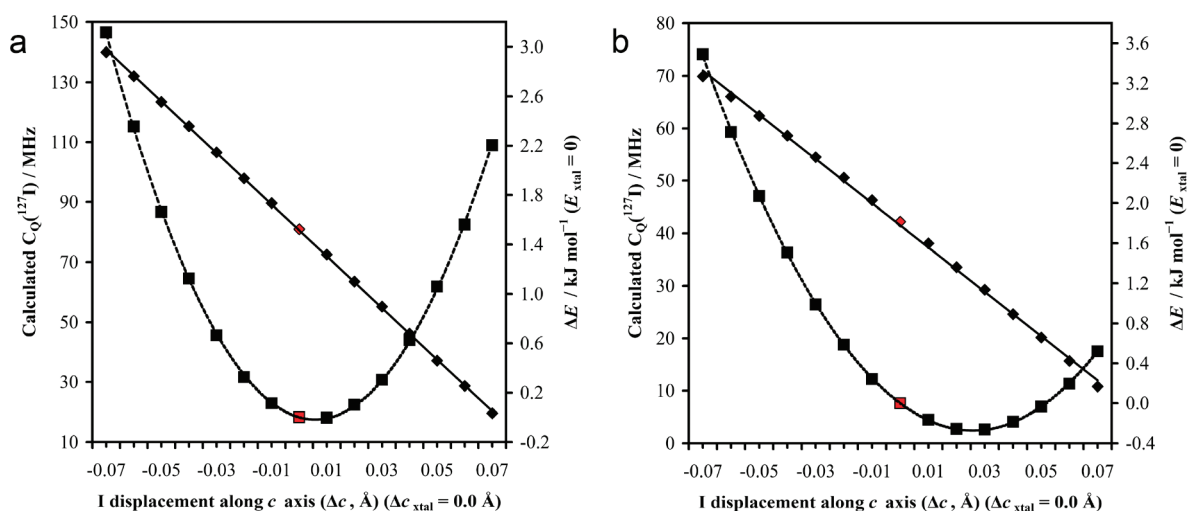


Figure 12. Plots of GIPAW DFT-computed $C_Q(^{127}\text{I})$ (left vertical axis, \blacklozenge) and relative energies (right vertical axis, \blacksquare) as functions of the iodide c -axis displacement in (a) MgI_2 and (b) CaI_2 . Relative energies are such that the energy associated with the accepted crystal structure ($E_{\text{xtal}} = 0$ kJ mol^{-1}). The c -axis displacements are such that the accepted crystal structure c displacement ($\Delta c_{\text{xtal}} = 0.0$ \AA). All calculations used $E_{\text{cut}} = 800$ eV, $9 \times 9 \times 6$ k -points, and the PBE XC functional. The lines of best fit are as follows: (a) $C_Q(^{127}\text{I}) = -861.0(\Delta c) + 80.58$, $R^2 = 0.9999$; $\Delta E = 543.6(\Delta c)^2 - 6.358(\Delta c) - 0.0005$, $R^2 = 0.9998$; (b) $C_Q(^{127}\text{I}) = -421.9(\Delta c) + 41.51$, $R^2 = 0.9988$; $\Delta E = 407.7(\Delta c)^2 - 21.08(\Delta c) - 0.0004$, $R^2 = 0.9999$. For each series, the data point corresponding to $\Delta c = 0$ is in red.

which is primarily due to the increase in the $\overline{r(\text{M}-\text{X})}$ value upon hydration. Finally, quantum chemical computations which employ the GIPAW DFT method reproduce the iodine \bar{V} parameters in these systems with a high degree of accuracy. These calculations also provide reasonable estimates of iodine δ_{iso} values, although the computed values are generally greater than those observed.

While the prohibitively large EFGs associated with covalent halides are likely to preclude routine observation using SSNMR experiments, it is nevertheless exciting to ponder the array of systems that halogen SSNMR experiments may be applied to when a halogen anion is present. For example, halogen anions may be intercalated into mesoporous materials, and the utility of ^{81}Br SSNMR experiments at probing these environments has very recently appeared in the literature.¹¹⁶ Perhaps the most interesting area of application for halogen NMR involves anion receptors¹¹⁷ (whether biological,¹¹⁸ biomimetic,¹¹⁹ organic,¹²⁰ etc.), where a number of weak interactions, such as $\text{X}^- \cdots \text{H}$ (hydrogen bonding), $\text{X}^- \cdots \text{X}$ (halogen bonding), and $\text{X}^- \cdots \pi$ work either individually or in tandem to stabilize the host anion(s). It will be interesting to see if halogen SSNMR

experiments can serve as useful probes of the weak interactions experienced in these systems.

Acknowledgment. D.L.B. thanks the Natural Sciences and Engineering Research Council (NSERC) of Canada for funding. C.M.W. thanks NSERC for an Alexander Graham Bell CGS D2 scholarship. Prof. Alex D. Bain (McMaster) is greatly thanked for providing us with a copy of his exact simulation software. Access to the 900 MHz NMR spectrometer was provided by the National Ultrahigh-Field NMR Facility for Solids (Ottawa, Canada), a national research facility funded by the Canada Foundation for Innovation, the Ontario Innovation Trust, Recherche Québec, the National Research Council Canada, and Bruker BioSpin and managed by the University of Ottawa (www.nmr900.ca). NSERC is acknowledged for a Major Resources Support grant. Dr. Eric Ye and Dr. Victor Tersikh are thanked for technical support at the 900 facility.

Supporting Information Available: Additional experimental details; detailed ^{127}I SSNMR acquisition parameters; GIPAW DFT calculations (pseudopotential files, energies, structure

references and parameters, additional information); additional ^{127}I SSNMR spectra and simulations (MgI_2 and BaI_2 (effect of Ω variation on line shape simulations), $\text{BaI}_2 \cdot 2\text{H}_2\text{O}$ (effects of sample grinding, ^1H decoupling, temperature variation)); ^{127}I NQR spectra (site I(2) in BaI_2 , $\text{SrI}_2 \cdot 6\text{H}_2\text{O}$); comparisons of ^{127}I SSNMR line shape simulations using second-order perturbation theory and exact theory (site I(1) in SrI_2 at 21.1 T, BaI_2 at 21.1 T, site I(2) in BaI_2 at 11.75 T, $\text{SrI}_2 \cdot 6\text{H}_2\text{O}$ at 21.1 T); halogen C_Q vs $Q(1 - \gamma_\infty)/V$ (BaX_2 series, $\text{SrX}_2 \cdot 6\text{H}_2\text{O}$ series); input parameters for calculations involving isostructural compounds and computed halogen C_Q and $Q(1 - \gamma_\infty)/V$ ratios; computed ^{127}I \vec{V} and $\vec{\sigma}$ eigenvectors (MgI_2 , CaI_2 , SrI_2 , BaI_2 , $\text{BaI}_2 \cdot 2\text{H}_2\text{O}$, $\text{SrI}_2 \cdot 6\text{H}_2\text{O}$, CdI_2 (4H)); normalized ^{127}I \vec{V} and $\vec{\sigma}$ eigenvector components in their crystal frames. This material is available free of charge via the Internet at <http://pubs.acs.org>.

References and Notes

- Housecroft, C. E.; Sharpe, A. G. In *Inorganic Chemistry*; Pearson Education Limited: Harlow, England, 2001; p 383.
- Shelton, P. A.; Zhang, Y.; Nguyen, T. H. H.; McElwee-White, L. *Chem. Commun.* **2009**, 947–949.
- Metrangolo, P.; Carcenac, Y.; Lahtinen, M.; Pilati, T.; Rissanen, K.; Vij, A.; Resnati, G. *Science* **2009**, 323, 1461–1464.
- Nicolaou, K. C.; Ellery, S. P.; Chen, J. S. *Angew. Chem., Int. Ed.* **2009**, 48, 7140–7165.
- Wirth, T. *Angew. Chem., Int. Ed.* **2005**, 44, 3656–3665.
- Kieltsch, I.; Eisenberger, P.; Togni, A. *Angew. Chem., Int. Ed.* **2007**, 46, 754–757.
- Harris, R. K.; Jackson, P. *Chem. Rev.* **1991**, 91, 1427–1440.
- Miller, J. M. *Prog. Nucl. Magn. Reson. Spectrosc.* **1996**, 28, 255–281.
- Ulrich, A. S. *Prog. Nucl. Magn. Reson. Spectrosc.* **2005**, 46, 1–21.
- Rossini, A. J.; Mills, R. W.; Briscoe, G. A.; Norton, E. L.; Geier, S. J.; Hung, I.; Zheng, S.; Autschbach, J.; Schurko, R. W. *J. Am. Chem. Soc.* **2009**, 131, 3317–3330.
- Hung, I.; Shetty, K.; Ellis, P. D.; Brey, W. W.; Gan, Z. *Solid State Nucl. Magn. Reson.* **2009**, 36, 159–163.
- Chapman, R. P.; Bryce, D. L. *Phys. Chem. Chem. Phys.* **2009**, 11, 6987–6998.
- Saito, T.; Inoue, H.; Tonisi, J.; Oosawa, A.; Goto, T.; Sasaki, T.; Kobayashi, N.; Awaji, S.; Watanabe, K. *J. Phys. Conf. Ser.* **2006**, 51, 203–206.
- Inoue, H.; Tani, S.; Hosoya, S.; Suzuki, T.; Goto, T.; Tanaka, H.; Sasaki, T.; Kobayashi, N. ^2D , $^{35/37}\text{Cl}$, $^{63/65}\text{Cu}$ -NMR Study of the Quantum Spin System NH_4CuCl_3 . *Low Temperature Physics: 24th International Conference on Low Temperature Physics*; American Institute of Physics: Melville, New York, 2006; Vol. 850, pp 1061–1062.
- Inoue, H.; Tani, S.; Hosoya, S.; Inokuchi, K.; Fujiwara, T.; Saito, T.; Suzuki, T.; Oosawa, A.; Goto, T.; Fujisawa, M.; Tanaka, H.; Sasaki, T.; Awaji, S.; Watanabe, K.; Kobayashi, N. *Phys. Rev. B* **2009**, 79, 174418.
- Imai, T.; Nytko, E. A.; Bartlett, B. M.; Shores, M. P.; Nocera, D. G. *Phys. Rev. Lett.* **2008**, 100, 077203.
- Tou, H.; Sera, M.; Maniwa, Y.; Yamanaka, S. *Int. J. Mod. Phys. B* **2007**, 21, 3340–3342.
- Bryce, D. L.; Sward, G. D.; Adiga, S. J. *Am. Chem. Soc.* **2006**, 128, 2121–2134.
- Chapman, R. P.; Bryce, D. L. *Phys. Chem. Chem. Phys.* **2007**, 9, 6219–6230.
- Gordon, P. G.; Brouwer, D. H.; Ripmeester, J. A. *J. Phys. Chem. A* **2008**, 112, 12527–12529.
- Gordon, P. G.; Brouwer, D. H.; Ripmeester, J. A. *Chem. Phys. Chem.* **2010**, 11, 260–268.
- Bryce, D. L.; Bultz, E. B. *Chem.—Eur. J.* **2007**, 13, 4786–4796.
- Vittadello, M.; Stallworth, P. E.; Alamgir, F. M.; Suarez, S.; Abbrent, S.; Drain, C. M.; Di Noto, V.; Greenbaum, S. G. *Inorg. Chim. Acta* **2006**, 359, 2513–2518.
- Hamaed, H.; Pawlowski, J. M.; Cooper, B. F. T.; Fu, R.; Eichhorn, S. H.; Schurko, R. W. *J. Am. Chem. Soc.* **2008**, 130, 11056–11065.
- Alonso, B.; Massiot, D.; Florian, P.; Paradies, H. H.; Gaveau, P.; Mineva, T. J. *Phys. Chem. B* **2009**, 113, 11906–11920.
- Widdifield, C. M.; Bryce, D. L. *J. Phys. Chem. A* **2010**, 114, 2102–2116.
- Widdifield, C. M.; Bryce, D. L. *Phys. Chem. Chem. Phys.* **2009**, 11, 7120–7122.
- Mizuno, M.; Iijima, T.; Kimura, J.; Endo, K.; Suhara, M. *J. Mol. Struct.* **2002**, 602–603, 239–244.
- Siegel, R.; Nakashima, T. T.; Wasylishen, R. E. *Concepts Magn. Reson. A* **2005**, 26A, 62–77.
- Wu, G.; Dong, S. *Solid State Nucl. Magn. Reson.* **2001**, 20, 100–107.
- Pyykkö, P. *Mol. Phys.* **2008**, 106, 1965–1974.
- Cohen, M. H.; Reif, F. *Solid State Phys.* **1957**, 5, 321–438.
- Ashbrook, S. E. *Phys. Chem. Chem. Phys.* **2009**, 11, 6892–6905.
- Bain, A. D. *Mol. Phys.* **2003**, 101, 3163–3175.
- Harris, R. K.; Becker, E. D.; Cabral De Menezes, S. M.; Granger, P.; Hoffman, R. E.; Zilm, K. W. *Pure Appl. Chem.* **2008**, 80, 59–84.
- Chapman, R. P.; Widdifield, C. M.; Bryce, D. L. *Prog. Nucl. Magn. Reson. Spectrosc.* **2009**, 55, 215–237.
- Solomon, I. *Phys. Rev.* **1958**, 110, 61–65.
- Weisman, I. D.; Bennett, L. H. *Phys. Rev.* **1969**, 181, 1341–1350.
- Kunwar, A. C.; Turner, G. L.; Oldfield, E. J. *Magn. Reson.* **1986**, 69, 124–127.
- Hahn, E. L. *Phys. Rev.* **1950**, 80, 580–594.
- Bhattacharyya, R.; Frydman, L. *J. Chem. Phys.* **2007**, 127, 194503.
- O'Dell, L. A.; Schurko, R. W. *Chem. Phys. Lett.* **2008**, 464, 97–102.
- Kupče, E.; Freeman, R. J. *Magn. Reson., Ser. A* **1995**, 115, 273–276.
- Massiot, D.; Farnan, I.; Gautier, N.; Trumeau, D.; Trokner, A.; Coutures, J. P. *Solid State Nucl. Magn. Reson.* **1995**, 4, 241–248.
- Medek, A.; Frydman, V.; Frydman, L. *J. Phys. Chem. A* **1999**, 103, 4830–4835.
- Schurko, R. W.; Wi, S.; Frydman, L. *J. Phys. Chem. A* **2002**, 106, 51–62.
- Eichele, K.; Wasylishen, R. E. *WSolids1: Solid-State NMR Spectrum Simulation Package*, v. 1.19.11; University of Tübingen: Tübingen, Germany, 2009.
- Buckingham, A. D.; Malm, S. M. *Mol. Phys.* **1971**, 22, 1127–1130.
- Robert, J. B.; Wiesenfeld, L. *Phys. Rep.* **1982**, 86, 363–401.
- Anet, F. A. L.; O'Leary, D. J. *Concepts Magn. Reson.* **1991**, 3, 193–214.
- Herzfeld, J.; Berger, A. E. *J. Chem. Phys.* **1980**, 73, 6021–6030.
- Mason, J. *Solid State Nucl. Magn. Reson.* **1993**, 2, 285–288.
- Jameson, C. J. *Solid State Nucl. Magn. Reson.* **1998**, 11, 265–268.
- Arfken, G. B.; Weber, H. J. *Euler Angles In Mathematical Methods for Physicists*; Academic Press: New York, 2005; Vol. 6, pp 202–203.
- Bryce, D. L. Tensor Interplay. In *NMR Crystallography*; Harris, R. K., Wasylishen, R. E., Duer, M. J., Eds.; John Wiley & Sons: West Sussex, U.K., 2009; pp 289–301.
- Semin, G. K. *Russ. J. Phys. Chem. A* **2007**, 81, 38–46.
- Livingston, R.; Zeldes, H. *ORNL-1913* **1955**, 26 pages.
- Pickard, C. J.; Mauri, F. *Phys. Rev. B* **2001**, 63, 245101.
- Yates, J. R.; Pickard, C. J.; Mauri, F. *Phys. Rev. B* **2007**, 76, 024401.
- Profeta, M.; Mauri, F.; Pickard, C. J. *J. Am. Chem. Soc.* **2003**, 125, 541–548.
- Clark, S. J.; Segall, M. D.; Pickard, C. J.; Hasnip, P. J.; Probert, M. I. J.; Refson, K.; Payne, M. C. *Z. Kristallogr.* **2005**, 220, 567–570.
- Vanderbilt, D. *Phys. Rev. B* **1990**, 41, 7892–7895.
- Perdew, J. P.; Burke, K.; Ernzerhof, M. *Phys. Rev. Lett.* **1996**, 77, 3865–3868.
- Perdew, J. P.; Burke, K.; Ernzerhof, M. *Phys. Rev. Lett.* **1997**, 78, 1396.
- Burke, K.; Perdew, J. P.; Wang, Y. In *Electronic Density Functional Theory: Recent Progress and New Directions*; Dobson, J. F., Vignale, G., Das, M. P., Eds.; Plenum: New York, 1998.
- Perdew, J. P. In *Electronic Structure of Solids '91*; Ziesche, P., Eschrig, H., Eds.; Akademie Verlag: Berlin, 1991; pp 11.
- Perdew, J. P.; Chevary, J. A.; Vosko, S. H.; Jackson, K. A.; Pederson, M. R.; Singh, D. J.; Fiolhais, C. *Phys. Rev. B* **1992**, 46, 6671–6687.
- Perdew, J. P.; Chevary, J. A.; Vosko, S. H.; Jackson, K. A.; Pederson, M. R.; Singh, D. J.; Fiolhais, C. *Phys. Rev. B* **1993**, 48, 4978.
- Perdew, J. P.; Burke, K.; Wang, Y. *Phys. Rev. B* **1996**, 54, 16533–16539.
- Herrmann, Z. Z. *Anorg. Allg. Chem.* **1931**, 197, 212–218.
- Agron, P. A.; Busing, W. R. *Acta Crystallogr., Sect. C* **1986**, C42, 141–143.
- Volkov, A. F. *Phys. Status Solidi B* **1972**, 50, K43–K44.
- Volkov, A. F. *J. Magn. Reson.* **1973**, 11, 73–76.
- Kellersohn, T.; Engelen, B.; Lutz, H. D.; Bartl, H.; Schweiss, B. P.; Fuess, H. Z. *Kristallogr.* **1991**, 197, 175–184.
- Blum, H. Z. *Phys. Chem. B* **1933**, B22, 298–304.
- Han, O. H.; Oldfield, E. *Inorg. Chem.* **1990**, 29, 3666–3669.
- Brogan, M. A.; Blake, A. J.; Wilson, C.; Gregory, D. H. *Acta Crystallogr., Sect. C* **2003**, C59, i136–i138.

- (78) Widdifield, C. M.; Schurko, R. W. *Concept. Magn. Reson. A* **2009**, 34A, 91–123.
- (79) Rietschel, E. T.; Bärnighausen, H. Z. *Anorg. Allg. Chem.* **1969**, 368, 62–72.
- (80) O'Dell, L. A.; Rossini, A. J.; Schurko, R. W. *Chem. Phys. Lett.* **2009**, 468, 330–335.
- (81) Widdifield, C. M.; Chapman, R. P.; Bryce, D. L. Chlorine, Bromine, and Iodine Solid-State NMR Spectroscopy; Webb, G. A., Ed.; *Annu. Rep. Nucl. Magn. Reson. Spectrosc.* 2009; Vol. 66, pp 195–326.
- (82) Creel, R. B.; Brooker, H. R.; Barnes, R. G. *J. Magn. Reson.* **1980**, 41, 146–149.
- (83) Abragam, A. *Principles of Nuclear Magnetism*; Oxford University Press: New York, 1961.
- (84) MacKenzie, K. J. D.; Smith, M. E. *Multinuclear Solid-State NMR of Inorganic Materials*; Pergamon: Amsterdam, 2002.
- (85) Bain, A. D. *J. Magn. Reson.* **2006**, 179, 308–310.
- (86) Gan, Z.; Srinivasan, P.; Quine, J. R.; Steuernagel, S.; Knott, B. *Chem. Phys. Lett.* **2003**, 367, 163–169.
- (87) Creel, R. B.; Drabold, D. A. *J. Mol. Struct.* **1983**, 111, 85–90.
- (88) Creel, R. B. *J. Magn. Reson.* **1983**, 52, 515–517.
- (89) Muha, G. M. *J. Magn. Reson.* **1983**, 53, 85–102.
- (90) Brackett, E. B.; Brackett, T. E.; Sass, R. L. *J. Phys. Chem.* **1963**, 67, 2132–2135.
- (91) Trigunayat, G. C.; Chadha, G. K. *Phys. Status Solidi A* **1971**, 4, 9–42.
- (92) Mitchell, R. S. Z. *Kristallogr.* **1956**, 108, 296–315.
- (93) Segel, S. L.; Barnes, R. G.; Jones, W. H., Jr. *Bull. Am. Phys. Soc.* **1960**, 5, 412.
- (94) Barnes, R. G.; Segel, S. L.; Jones, W. H., Jr. *J. Appl. Phys.* **1962**, 33, 296–302.
- (95) Lyfar, D. L.; Goncharuk, V. E.; Ryabchenko, S. M. *Phys. Stat. Sol. B* **1976**, 76, 183–189.
- (96) Nolle, A. Z. *Naturforsch. A* **1978**, 33, 666–671.
- (97) Ellis, P. D. *Science* **1983**, 221, 1141–1146.
- (98) Sakida, S.; Kawamoto, Y. *J. Phys. Chem. Solids* **2002**, 63, 151–161.
- (99) Ramsey, N. F. *Phys. Rev.* **1950**, 78, 699–703.
- (100) Ramsey, N. F. *Phys. Rev.* **1951**, 83, 540–541.
- (101) Ramsey, N. F. *Physica (The Hague)* **1951**, 17, 303–307.
- (102) Sternheimer, R. *Phys. Rev.* **1950**, 80, 102.
- (103) Sternheimer, R. *Phys. Rev.* **1951**, 84, 244.
- (104) Lucken, E. A. C. Sternheimer Shielding. In *Nuclear Quadrupole Coupling Constants*; Academic Press: London, 1969; pp 79–96.
- (105) Wu, G.; Tersikh, V. *J. Phys. Chem. A* **2008**, 112, 10359–10364.
- (106) Yamagata, Y. *J. Phys. Soc. Jpn.* **1964**, 19, 10–23.
- (107) Hayashi, S.; Hayamizu, K. *Bull. Chem. Soc. Jpn.* **1990**, 63, 913–919.
- (108) Jameson, C. J.; Gutowsky, H. S. *J. Chem. Phys.* **1964**, 40, 1714–1724.
- (109) Ashbrook, S. E.; Berry, A. J.; Frost, D. J.; Gregorovic, A.; Pickard, C. J.; Readman, J. E.; Wimperis, S. *J. Am. Chem. Soc.* **2007**, 129, 13213–13224.
- (110) Bryce, D. L.; Bultz, E. B.; Aebi, D. *J. Am. Chem. Soc.* **2008**, 130, 9282–9292.
- (111) Hamaed, H.; Laschuk, M. W.; Tersikh, V. V.; Schurko, R. W. *J. Am. Chem. Soc.* **2009**, 131, 8271–8279.
- (112) Cahill, L. S.; Hanna, J. V.; Wong, A.; Freitas, J. C. C.; Yates, J. R.; Harris, R. K.; Smith, M. E. *Chem.—Eur. J.* **2009**, 15, 9785–9798.
- (113) Sutrisno, A.; Lu, C.; Lipson, R. H.; Huang, Y. *J. Phys. Chem. C* **2009**, 113, 21196–21201.
- (114) Moudrakovski, I.; Lang, S.; Patchkovskii, S.; Ripmeester, J. *J. Phys. Chem. A* **2010**, 114, 309–316.
- (115) Hanna, J. V.; Pike, K. J.; Charpentier, T.; Kemp, T. F.; Smith, M. E.; Lucier, B. E. G.; Schurko, R. W.; Cahill, L. S. *Chem.—Eur. J.* **2010**, 16, 3222–3239.
- (116) Alonso, B.; Mineva, T.; Innocenzi, P.; Trimmel, G.; Stubenrauch, K.; Melnyk, I.; Zub, Y.; Fayon, F.; Florian, P.; Massiot, D. *C. R. Chim.* **2010**, 13, 431–442.
- (117) Caltagirone, C.; Gale, P. A. *Chem. Soc. Rev.* **2009**, 38, 520–563.
- (118) Kawakami, K.; Umena, Y.; Kamiya, N.; Shen, J. R. *Proc. Natl. Acad. Sci. U.S.A.* **2009**, 106, 8567–8572.
- (119) Sansone, F.; Baldini, L.; Casnati, A.; Lazzarotto, M.; Ugozzoli, F.; Ungaro, R. *Proc. Natl. Acad. Sci. U.S.A.* **2002**, 99, 4842–4847.
- (120) Saeed, M. A.; Fronczek, F. R.; Hossain, M. A. *Chem. Commun.* **2009**, 6409–6411.
- (121) Bondi, A. *J. Phys. Chem.* **1964**, 68, 441–451.
- (122) Mantina, M.; Chamberlin, A. C.; Valero, R.; Cramer, C. J.; Truhlar, D. G. *J. Phys. Chem. A* **2009**, 113, 5806–5812.
- (123) Jameson, C. J.; Mason, J. The Chemical Shift. In *Multinuclear NMR*; Mason, J., Ed.; Plenum Press: New York, 1987; pp 59–65.